HHS Public Access

Author manuscript

Nat Immunol. Author manuscript; available in PMC 2024 May 16.

Published in final edited form as:

Nat Immunol. 2023 October ; 24(10): 1685–1697. doi:10.1038/s41590-023-01620-z.

Control of nutrient uptake by IRF4 orchestrates innate immune memory

Endi K. Santosa[1,2], **Hyunu Kim**[1], **Timo Rückert**[3], **Jean-Benoît Le Luduec**[1], **Aamna J. Abbasi**[1], **Claire K. Wingert**[1], **Lila Peters**[1], **Joe N. Frost**[1], **Katharine C. Hsu**[1,4,5], **Chiara Romagnani**[3,6,7], **Joseph C. Sun**[1,2,✉]

[1]Immunology Program, Memorial Sloan Kettering Cancer Center, New York, NY, USA.

[2]Department of Immunology and Microbial Pathogenesis, Weill Cornell Medical College, New York, NY, USA.

[3]Innate Immunity, Deutsches Rheuma-Forschungszentrum Berlin (DRFZ), ein Leibniz Institut, Berlin, Germany.

[4]Department of Medicine, Memorial Sloan Kettering Cancer Center, New York, NY, USA.

[5]Department of Medicine, Weill Cornell Medical College, New York, NY, USA.

[6]Charité – Universitätsmedizin Berlin, Corporate Member of Freie Universität Berlin and Humboldt Universität zu Berlin, Berlin, Germany.

[7]Leibniz-Science Campus Chronic Inflammation, Berlin, Germany.

Abstract

Natural killer (NK) cells are innate cytotoxic lymphocytes with adaptive immune features, including antigen specificity, clonal expansion and memory. As such, NK cells share many transcriptional and epigenetic programs with their adaptive $CD8^+$ T cell siblings. Various signals ranging from antigen, co-stimulation and proinflammatory cytokines are required for optimal NK cell responses in mice and humans during virus infection; however, the integration of these signals remains unclear. In this study, we identified that the transcription factor IRF4 integrates signals to coordinate the NK cell response during mouse cytomegalovirus infection. Loss of IRF4 was detrimental to the expansion and differentiation of virus-specific NK cells. This defect was

✉Correspondence and requests for materials should be addressed to Joseph C. Sun, sunj@mskcc.org.

Author contributions

E.K.S. and J.C.S. designed the study. E.K.S., H.K., J.-B.L.L., A.J.A., C.K.W., L.P. and J.N.F. performed experiments. E.K.S. and T.R. performed bioinformatics analyses. K.C.H., C.R. and J.C.S. provided critical resources and supervision for the study. E.K.S. and J.C.S. wrote the manuscript.

Competing interests

The authors declare no competing interests.

Additional information

Extended data is available for this paper at https://doi.org/10.1038/s41590-023-01620-z.

Supplementary information The online version contains supplementary material available at https://doi.org/10.1038/s41590-023-01620-z.

Peer review information *Nature Immunology* thanks Dagmar Gotthardt and the other, anonymous, reviewer(s) for their contribution to the peer review of this work.

partially attributed to the inability of IRF4-deficient NK cells to uptake nutrients required for survival and memory generation. Altogether, these data suggest that IRF4 is a signal integrator that acts as a secondary metabolic checkpoint to orchestrate the adaptive response of NK cells during viral infection.

Host defense against viral infection requires a coordinated response by both innate and adaptive immunity. NK cells are innate cytotoxic lymphocytes that share many transcriptional and epigenetic programs with their adaptive counterparts, $CD8^+$ T cells[1]. Although NK cells are an indispensable component of innate immunity due to their rapid cytolytic and immunoregulatory functions, recent findings in mice, humans and nonhuman primates have suggested that NK cells also contribute to adaptive immunity and possess features similar to $CD8^+$ T cells, including antigen specificity, clonal expansion and the ability to generate immunological memory[2,3].

Multiple factors are critical for the innate and adaptive responses of NK cells to viral infection. Similar to T cells, these NK cell signals include 'antigen' engagement[4,5], co-stimulation[6] and proinflammatory cytokines[7–11]. For example, during cytomegalovirus infection, the engagement of activating receptors Ly49H or NKG2C on subsets of mouse or human NK cells, respectively, along with the presence of homeostatic and proinflammatory cytokines, imprint transcriptional and epigenetic programs that dictate the innate and adaptive responses of NK cells[1,12]. Nevertheless, how this multitude of signals is integrated to drive NK cell adaptive responses remains to be explored.

The interferon regulatory factor (IRF) is a transcription factor family consisting of nine members whose expression and function are primarily regulated by type I, II and III interferons (IFNs)[13]; however, at least two of the IRF family members, IRF4 and IRF8, are induced by additional stimuli and play important roles in the development, differentiation and function of immune cells, including dendritic cells, plasma cells and T cells[14,15]. Previous studies have reported that the development of NK cells is perturbed in IRF1- and IRF2-deficient mice[16–18]. More recently, several studies have also identified the role of IRF8 in human and mouse NK cells. Patients with biallelic *IRF8* mutations are highly susceptible to viral infection, in part due to diminished NK cell numbers, maturation and cytolytic functions[19]. Furthermore, NK cell-specific IRF8 deficiency in mice results in the cell-intrinsic inability of NK cells to undergo clonal expansion following mouse cytomegalovirus (MCMV) infection due to its role in directly controlling the expression of the transcription factor *Zbtb32* (refs. 20,21).

Although rare, IRF4 deficiency in humans results in primary immunodeficiency with abnormally low counts of activated B cells, regulatory T cells and effector and memory $CD4^+$ and $CD8^+$ T cells; this global immune defect is similarly observed in the IRF4-deficient mouse model[15,22,23]; however, a role for IRF4 in innate lymphocyte development or function has not been described. In this study, we observed that IRF4 is dynamically upregulated in NK cells upon cytomegalovirus (CMV) infection in both mice and humans and its induction requires inputs from both activating receptor and proinflammatory cytokines. NK cell-intrinsic IRF4 expression was required for antiviral immunity by regulating the survival of differentiating NK cells during infection. Finally, IRF4 controlled

the uptake of nutrients needed for the adaptive response of NK cells. Collectively, our findings suggest that the transcription factor IRF4 acts as a signal integrator and secondary metabolic checkpoint to promote robust antiviral NK cell responses.

Results

NK cells upregulate IRF4 in response to viral infection

NK cells can express several IRF family members during viral infection (Extended Data Fig. 1a) and the differential induction and contribution of IRF8 and IRF9 in antiviral NK cell responses have been previously described[20,24]. Here, we observed that IRF4 is highly upregulated in Ly49H$^+$ NK cells early after MCMV infection (Fig. 1a), with transcript and protein levels peaking on days 2 and 3 post-infection (PI), respectively (Fig. 1b,c and Extended Data Fig. 1b). Consistent with IRF4 transcript and protein expression, we also observed that the *Irf4* locus is dynamically regulated during the course of infection as assessed by ATAC-seq, with several chromatin accessible regions maintaining their 'openness' after infection (Extended Data Fig. 1c). Although IRF4 expression in activated Ly49H$^+$ NK cells peaked at 2–3 d PI, ATAC-seq analysis of highly accessible regions ($\log_2$fold change (FC) ≥ 1, adjusted *P* value (P_{adj}) < 0.05) demonstrated that IRF4, AP-1 and IRF:bZIP motifs are enriched on day 4 PI (Extended Data Fig. 1d,e), suggesting a functional cooperation between IRF4 and AP-1 factors and a slight delay between IRF4 expression and IRF4-driven transcriptional and epigenetic programs.

Human CMV (HCMV) infection can induce the expansion of a NKG2C$^+$ NK cell subset that exhibits adaptive features[25]. As such, this unique adaptive NKG2C$^+$ NK cell subset in humans is thought to be analogous to the MCMV-specific Ly49H$^+$ NK cells found in mice. Given the similarities between mouse and human NK cell responses to CMV, we sought to investigate whether IRF4 is also induced in human NK cells during their response to HCMV. To do so, we analyzed transcriptomic and chromatin accessibility datasets of human NK cells from HCMV-seropositive individuals. Single-cell ATAC-sequencing (scATAC-seq) data[26] revealed that adaptive NK cells (NKG2C$^+$CD56^{dim}) are epigenetically distinct from less-mature CD56^{bright}, early CD56^{dim} and conventional CD56^{dim} NK cells (Fig. 1d). This distinct epigenetic signature is partly associated with high accessibility of the *IRF4* promoter within this adaptive NKG2C$^+$ NK cell subset compared to other NK cell populations (Fig. 1e), consistent with our observation in mouse Ly49H$^+$ NK cells responding to MCMV (Extended Data Fig. 1c). RNA-seq analysis from a separate study also suggested that *IRF4* transcripts are highest in the adaptive NKG2C$^+$ NK subset (Fig. 1f)[27]. Moreover, whereas induction of IRF8 and IRF9 are primarily dependent on the IL-12–STAT4 and type I IFN–STAT1 axes, respectively[20,24], optimal expression of IRF4 in NK cells required synergistic signals from an activating receptor in addition to homeostatic and proinflammatory cytokines in both mice and humans (Fig. 1g,h and Extended Data Fig. 1f–i). Thus, IRF4 may act as a conserved 'hub' for integrating multiple signals during the antiviral NK cell response across species.

IRF4 is critical for NK cell-mediated antiviral immunity

Because IRF4-deficient mice are immunocompromised due to developmental defects in multiple immune and non-immune cells that may impact NK cell homeostasis, we first characterized the NK cell compartment in *Irf4*$^{-/-}$ mice and their littermate controls. Our analysis revealed that *Irf4*$^{-/-}$ mice exhibited similar NK cell number and maturation states compared to their *Irf4*$^{+/-}$ and wild-type (WT) littermates (Extended Data Fig. 2a–f). Notably, we observed a slightly lower proportion of Ly49H^{+} NK cells in these mice (Extended Data Fig. 2g). To determine whether this defect was cell-intrinsic, we generated WT (CD45.1):*Irf4*$^{-/-}$ (CD45.2) mixed bone-marrow chimera mice (mBMC). Consistent with a previous report[28] and our own findings, we found no developmental and maturation defects in *Irf4*$^{-/-}$ NK cells in this setting (Extended Data Fig. 2h–m) and no longer observed differences in Ly49H^{+} NK cell proportion (Extended Data Fig. 2n), suggesting cell-extrinsic factors may control Ly49H expression in the *Irf4*$^{-/-}$ mice. Furthermore, we also observed no evidence of defective expansion or maturation of *Irf4*$^{-/-}$ NK cells adoptively transferred into lymphopenic *Rag2*$^{-/-}$*Il2rg*$^{-/-}$ mice in the absence of infection (Extended Data Fig. 3). Together, these data suggest that NK cell development, maturation and homeostatic proliferation are not dependent on IRF4.

To assess the NK cell-intrinsic contribution of IRF4 in mediating antiviral defense, we used a well-established adoptive transfer system[3], where an equal number of purified WT or *Irf4*$^{-/-}$Ly49H^{+} NK cells were transferred into separate *Rag2*$^{-/-}$*Il2rg*$^{-/-}$ mice (which lack all lymphocytes) and recipients were challenged with MCMV. In contrast to mice that received WT Ly49H^{+} NK cells, recipients receiving *Irf4*$^{-/-}$Ly49H^{+} NK cells rapidly succumbed to MCMV, similar to *Rag2*$^{-/-}$*Il2rg*$^{-/-}$ mice that received no cells (Fig. 2a), suggesting that NK cell-intrinsic IRF4 is required for host protection against MCMV.

To understand why *Irf4*$^{-/-}$ NK cells failed to protect against MCMV infection, we first assessed the effector functions of NK cells. In response to IL-12 + IL-18, PMA + ionomycin, or PMA + ionomycin + IL-12, *Irf4*$^{-/-}$ NK cells were able to produce the immunoregulatory cytokine IFN-γ and degranulate comparably to WT NK cells (Extended Data Fig. 4a,b). Furthermore, we observed no difference in the expression of activation markers CD25 and CD69, or the production of IFN-γ and cytolytic molecule granzyme B, following MCMV infection in vivo (Extended Data Fig. 4c–f). Thus, IRF4 seems dispensable for early NK cell activation and innate effector functions.

We then tested whether IRF4 is required for the expansion of virus-specific NK cells. To do so, we adoptively transferred equal numbers of WT (CD45.1) and *Irf4*$^{-/-}$ (CD45.2) Ly49H^{+} NK cells into Ly49H-deficient mice and challenged these recipient mice with MCMV. This system allows for longitudinal monitoring of the expansion and memory formation of WT and *Irf4*-deficient Ly49H^{+} NK cells within the same host. Whereas WT Ly49H^{+} NK cells expanded robustly by day 7 PI, their *Irf4*$^{-/-}$ counterparts failed to expand and thus contributed to a much smaller pool of memory cells 30 days later (Fig. 2b). Moreover, this expansion defect of *Irf4*$^{-/-}$ NK cells was also observed across multiple different tissues, including blood, spleen and liver (Fig. 2c).

To determine whether the expansion defect of *Irf4*$^{-/-}$ NK cells was caused by a failure to proliferate, we labeled WT and *Irf4*$^{-/-}$Ly49H^{+} NK cells with CellTrace Violet (CTV) before transfer and infection. Consistent with similar observations in CD8^{+} T cells, *Irf4*$^{-/-}$Ly49H^{+} NK cells were capable of dividing comparably with WT Ly49H^{+} NK cells based on CTV dilution (Fig. 2d)[23,29]; however, activated *Irf4*$^{-/-}$ NK cells failed to downregulate the pro-apoptotic molecule BIM compared to WT NK cells (Fig. 2e). As a result, *Irf4*$^{-/-}$ NK cells had a higher BIM expression compared to WT NK cells and were more sensitive to cell death upon treatment with a BCL2 inhibitor (Fig. 2f). Hence, these data suggest that IRF4 controls NK cell survival during viral infection by regulating BIM expression.

IRF4 regulates effector differentiation of NK cells

To investigate whether IRF4 promotes differentiation of activated NK cells, we profiled WT and *Irf4*$^{-/-}$Ly49H^{+} NK cell subsets from various tissues at day 7 PI. We found that *Irf4*$^{-/-}$ NK cells possessed a higher proportion of the immature cell fraction (CD27^{+}CD62L^{+}) compared to WT across all tissues and a profound loss of mature cells (CD27^{-}CD62L^{-}) (Fig. 3a)[30]. Moreover, *Irf4*$^{-/-}$ NK cells showed a reduction in maturation markers Ly6C and CX_3CR1 and a slight decrease in KLRG1 expression compared to WT NK cells (Fig. 3b). Altogether, these data suggest that IRF4 controls NK cell differentiation during infection and contributes to the heterogeneity of the adaptive NK cell response.

To better understand when exactly IRF4 exerts its function, we infected WT:*Irf4*$^{-/-}$ mBMC mice with MCMV and phenotypically characterized the Ly49H^{+} NK cell compartment with a tight kinetic window, namely on days 0, 2, 4, 5 and 7 PI. In the mBMC setting, progressive loss of *Irf4*$^{-/-}$Ly49H^{+} NK cells began on day 4 and continued to decline until day 7 PI (Fig. 3c). Consistent with our observations in the adoptive transfer setting, phenotypic profiling of WT and *Irf4*$^{-/-}$ NK cells based on CD27 and CD62L showed an accumulation of immature double-positive (CD27^{+}CD62L^{+}) cells on day 4 until day 7 PI, which coincided with a severe reduction in the mature double negative (CD27^{-}CD62L^{-}) proportion of *Irf4*$^{-/-}$ NK cells (Fig. 3d). Thus, IRF4 likely regulates a transcriptional program that controls NK cell survival and differentiation early after viral infection.

Next, we performed single-cell RNA-sequencing (scRNA-seq) on WT versus *Irf4*$^{-/-}$ Ly49H^{+} NK cells on day 0, 2, 4 and 7 following MCMV infection. Unsupervised Louvain clustering (k_n = 30) identified 12 clusters that mostly delineate the kinetics of infection. Naive NK cells (day 0) are represented by clusters 0 and 4, NK cells on day 2 PI are identified by clusters 7, 9 and 11, NK cells on day 4 PI are demarcated by clusters 2, 5, 6 and 8, and clusters 1 and 3 are enriched for NK cells from day 7 PI (Fig. 4a and Extended Data Fig. 5a). Notably, cluster 1 is dominated by WT NK cells from day 7 PI, whereas *Irf4*$^{-/-}$ NK cells from day 7 PI consist of the largest population in cluster 3 (Extended Data Fig. 5b).

Differential expression analysis by MAST[31] showed very few differences in gene expression on day 0 and day 2 PI between the two groups (Extended Data Fig. 5c,d), but did confirm loss of *Irf4* expression in the *Irf4*$^{-/-}$ NK cells compared to WT cells on day 2 PI (Extended Data Fig. 5c). Analysis of Top 50 most differentially expressed genes (DEGs) illustrates distinct gene expression patterns between WT and *Irf4*$^{-/-}$ NK cells on day 7 PI (Fig. 4b)

and globally, partition-based graph abstraction (PAGA) analysis also suggests that *Irf4*$^{-/-}$ NK cells from day 7 PI are more closely related to naive NK cells than WT NK cells on day 7 PI (Fig. 4c). Moreover, the number of genes that are differentially expressed between WT and *Irf4*$^{-/-}$ NK cells increased to 62 genes on day 4 PI and to 2,178 genes by day 7 PI ($P_{adj} < 0.05$) (Extended Data Fig. 5c,d), which is consistent with the Uniform Manifold Approximation and Projection (UMAP) embedding on day 7 PI where WT and *Irf4*$^{-/-}$ cells are most segregated from one another (Fig. 4d). Among genes that were found to be significantly dysregulated in *Irf4*$^{-/-}$ NK cells compared to WT cells, many have been implicated in the differentiation of NK cells and effector CD8^{+} T cells (for example *Tbx21*, *Eomes*, *Zeb2*, R*unx1*, *Runx3*, *Id2* and *Fli1*) or are associated with lymphocyte maturation (Fig. 4e,f)[32–39]. Gene score analysis also confirmed that *Irf4*$^{-/-}$ NK cells from day 7 PI are enriched in genes associated with 'memory precursor' effector cells (MPECs), whereas the WT NK cell cluster exhibited a greater 'short-lived' effector cell (SLEC) signature (Fig. 4g). Furthermore, we also confirmed that *Irf4*$^{-/-}$ NK cells failed to downregulate BIM (encoded by *Bcl2l11*) at the transcript level compared to WT cells (Fig. 4e), possibly due to direct suppression of BIM by IRF4 (ref. 29). Altogether, these data suggest that IRF4 drives a transcriptional program that regulates the survival and differentiation of NK cells during viral infection.

IRF4 controls nutrient uptake for adaptive NK cell responses

Gene set enrichment analysis (GSEA) pathway analysis of DEGs between WT and *Irf4*$^{-/-}$ NK cells on day 7 PI also suggested that WT cells are enriched for genes involved in metabolic processes (for example oxidative phosphorylation) and genes known to be regulated by MYC (Fig. 5a). MYC itself is upregulated early after infection, but there was no difference in MYC expression at transcript and protein levels between WT and *Irf4*$^{-/-}$ NK cells (Extended Data Fig. 5e,f); however, the expression of known MYC targets, namely CD98 and CD71, are significantly dysregulated in the *Irf4*$^{-/-}$ NK cells during infection (Fig. 5b,c and Extended Data Fig. 5g), suggesting additional layers of regulation either independent of or in cooperation with MYC, but not entirely dependent on MYC.

CD98, encoded by *Slc3a2*, is a heterodimer partner of LAT1 (*Slc7a5*) and is needed to regulate the intake of large L-type neutral amino acids[40], whereas CD71, also known as transferrin receptor (*Tfrc*), plays an important role in iron uptake. As such, failure to acquire iron has been shown to dramatically impact innate and adaptive immunity to various infections[41–43]. To determine whether reduced CD98 expression impacts the capacity of *Irf4*$^{-/-}$ NK cells to uptake large neutral amino acids, we analyzed their ability to take up kynurenine, a fluorescent neutral amino acid analog. Compared to WT NK cells, *Irf4*$^{-/-}$ NK cells showed a reduction in kynurenine uptake (Fig. 5d). The addition of a neutral amino acid-competitor (leucine) reduced the overall kynurenine uptake, but *Irf4*$^{-/-}$ NK cells still showed diminished uptake of kynurenine compared to WT NK cells in this setting (Fig. 5d). Similarly, to assess the function of CD71 in WT versus *Irf4*$^{-/-}$Ly49H^{+} NK cells, we performed an ex vivo transferrin uptake assay and found no difference in transferrin uptake between naive WT and *Irf4*$^{-/-}$ populations (Fig. 5e); however, during MCMV infection, WT NK cells readily took up transferrin in contrast to *Irf4*$^{-/-}$ NK cells, whose transferrin uptake was impaired (Fig. 5e). Collectively, our findings suggest that IRF4 controls the ability of

NK cells to take up multiple nutrients that may be necessary for optimal antiviral NK cell responses.

Given that *Irf4*$^{-/-}$ NK cells are less capable of taking up these nutrients, we tested how the availability of these nutrients affects the adaptive NK cell response. First, we treated MCMV-infected WT mice with PBS or BCH, a LAT1-CD98 inhibitor (Extended Data Fig. 6a). Interestingly, infected mice treated with BCH did not show any alterations in NK cell adaptive response, as assessed by cell number and maturation markers CD27 and CD62L compared to the PBS-treated group, suggesting that large neutral amino acid uptake by LAT1 is not required for NK cell expansion and differentiation during the adaptive NK cell response (Extended Data Fig. 6b,c). We also assessed the contribution of iron in driving these processes by treating MCMV-infected WT mice with either PBS or deferiprone, an iron chelator (Fig. 6a). We observed that deferiprone induced cellular iron deficiency in NK cells responding to MCMV as evidenced by increased CD71 expression (Extended Data Fig. 6d). In contrast to LAT1-CD98 inhibition, deferiprone-treated mice showed a severe reduction in antiviral NK cell expansion by both proportion and cell number in blood, liver and spleen (Fig. 6b,c). Additionally, whereas Ly49H^{+} NK cells from PBS-treated mice could differentiate into mature CD27^{-}CD62L^{-} cells, deferiprone-treated NK cells were enriched for immature cells, similar to *Irf4*$^{-/-}$ NK cells (Figs. 3a and 6d). Furthermore, Ly49H^{+} NK cells from deferiprone-treated mice showed dysregulation of maturation markers such as CX_3CR1 and KLRG1 and maintained high levels of BIM compared to the control group (Fig. 6e,f and Extended Data Fig. 6e–g). Last, we observed no significant differences in proliferation (based on Ki-67 staining) between the PBS- or deferiprone-treated groups (Fig. 6g). Because the phenotypes observed in *Irf4*$^{-/-}$ NK cells are well recapitulated in deferiprone-treated mice, we hypothesize that the disruption in iron uptake observed in *Irf4*$^{-/-}$ NK cells contributes to the defect in the adaptive response of antiviral NK cells.

IRF4 directly regulates adaptive features of NK cells

To gain further insights into the direct transcriptional regulation of NK cells by IRF4, we performed chromatin immunoprecipitation followed by sequencing (ChIP-seq) on NK cells stimulated through NK1.1 and proinflammatory cytokines. We identified a total of 12,344 IRF4-binding peaks with the majority of these peaks found specifically in the stimulated condition (n = 10,795 peaks) compared to unstimulated control (Fig. 7a). Notably, we observed direct binding of IRF4 to the *Bcl2l11* and *Sell* loci, indicating its direct regulation of cellular survival and differentiation, respectively (Fig. 7b). In addition, we also observed strong direct binding of IRF4 to the *Tfrc* and *Ireb2* loci, which encode for components of the iron uptake machinery (Fig. 7b). Thus, these observations highlight the involvement of IRF4 in directly regulating NK cell survival, differentiation and nutrient uptake for the adaptive NK cell response.

To gain a global understanding into how IRF4 regulates the transcriptional landscape of differentiating NK cells in response to MCMV, we compared genes bound by IRF4 with DEGs from WT and *Irf4*$^{-/-}$Ly49H^{+} NK cells on day 7 PI. Remarkably, we found that nearly 40% of DEGs were direct targets of IRF4 and the majority of these IRF4-bound DEGs were upregulated in *Irf4*$^{-/-}$ NK cells, suggesting that IRF4 primarily acts as a transcriptional

repressor during NK cell differentiation following viral infection (Fig. 7c). Furthermore, we found that IRF4 occupancy is predominantly enriched in the intronic and intergenic regions, with lower representation in promoters and exons (Fig. 7d), suggesting a preferential binding of IRF4 to putative distal enhancers.

Moreover, motif enrichment analysis reveals that AP-1 and AICE (AP-1-IRF composite element), along with IRF motifs, were highly enriched in IRF4-bound sites upon stimulation (Fig. 7e), suggesting a potential interaction of IRF4 with AP-1 factors in controlling optimal NK cell responses, similar to what has been observed for T cells[44]. Given that the accessibility of chromatin plays a critical role in the binding of transcription factors to their target sites, we next investigated how IRF4 binding might be affected by the chromatin accessibility of these motifs throughout NK cell differentiation following MCMV infection. From this analysis, we found that regions bound by IRF4 that contain AP-1, AICE and IRF motifs are highly accessible on day 2 and day 4 PI compared to the other time points, with AICE motif-containing regions exhibited comparable accessibility on day 2 and day 4 PI (Fig. 7f), suggesting that the temporal binding of IRF4 to the chromatin may be facilitated and is occurring during the day 2 to 4 PI window.

Lastly, to investigate the regulatory network of AICE motif-containing genes controlled by IRF4 in NK cells during MCMV infection, we focused on the expression patterns of IRF4-bound AICE motif-containing genes that show differential expression at any time point throughout infection (n = 686 genes) (Fig. 7g). We then performed GSEA analysis using the DEGs between WT versus *Irf4*$^{-/-}$ NK cells at all time points as customized ‘pathways’ and plotted the average expression of genes enriched in each category. Consistent with its role as transcriptional repressor, AICE motif-containing genes enriched in the absence of IRF4 are repressed following infection, whereas those that are enriched in WT NK cells showed upregulation on day 4 PI and maintained their expression thereafter (Fig. 7g), suggesting that the interaction between IRF4 and AP-1 factors may together act as a transcriptional repressor orchestrating the differentiation of effector and memory NK cells in response to viral infection.

Discussion

The transition of naive to effector and memory NK cells requires the stepwise acquisition of a transcriptional circuitry that involves suppression of the naive NK cell identity and upregulation of NK cell effector and memory programs. While the molecular pathways that drive naive lymphocyte differentiation into various effector and memory subsets have been extensively studied in T and B cells[45,46], these pathways are only beginning to be unraveled in NK cells. Recent studies showed that antiviral Ly49H^{+} NK cells are phenotypically and functionally heterogeneous following MCMV infection based on the expression of various markers, including CD27, CD62L, Ly6C and Ly49H itself[30,36,47,48]. Furthermore, the transcription factor Fli1 was recently implicated in controlling NK cell functional heterogeneity by restricting the formation of ‘memory precursor’ NK cells[36]. In the present study, we demonstrate that the transcription factor IRF4 drives the effector differentiation and survival of virus-specific NK cells during MCMV infection. In our hands, loss of IRF4 results in an aberrant effector differentiation program in NK cells that

is characterized by an MPEC-like state but distinct from the naive NK cell program, as highlighted by the dysregulation of the transcription factor network known to control NK cell maturation and effector CD8$^+$ T cell differentiation, involving genes such as *Tbx21*, *Zeb2*, *Id2* and *Eomes*[32–34,49]. Importantly, this requirement for IRF4 is specific to viral infection, as steady-state NK cell maturation and lymphopenia-driven proliferation were unaffected by the loss of IRF4. Moreover, our findings establish a parallel between the role of IRF4 in promoting effector and memory differentiation in NK cells and its role in promoting effector CD8$^+$ T cell differentiation, which may suggest a common underlying mechanism of cytotoxic lymphocytes responses to viral infection.

Paradoxically, deficiencies in Eomes or Id2 in steady-state NK cells and effector CD8$^+$ T cells result in an accumulation of immature NK cells and MP-like CD8$^+$ T cell subsets, respectively[35,39,50,51], reminiscent of our observations with *Irf4*$^{-/-}$ NK cells; however, unlike CD8$^+$ T cells that upregulate *Id2* and *Eomes* during their differentiation to effector cells, the transition of naive NK cells into memory cells is associated with the downregulation of these transcription factors, whereas ectopic expression of these factors during stage-specific transitions may interfere with the proper differentiation of activated NK cells during viral infection. Thus, our findings may hint at distinct mechanisms that distinguish steady-state NK cell development and maturation, as well as CD8$^+$ T cell effector differentiation from the acquisition of NK cell effector and memory programs.

Although coordinated transcriptional circuitry is certainly critical for optimal lymphocyte responses, the differentiation and expansion of adaptive NK cells during viral infection also requires metabolic adaptations and sufficient nutrient uptake to sustain these metabolically taxing processes[52–54]. What is less clear is how NK cell metabolism is synchronized with dynamic changes in differentiation state during infection. Here we show that IRF4 is necessary for sustained nutrient intake during the adaptive phase of the NK cell response. In particular, our data demonstrate a new role of IRF4 in controlling intracellular iron acquisition and homeostasis through direct transcriptional regulation of genes that encode for iron acquisition machinery, including *Tfrc* and *Ireb2* (which encode for CD71 and IRP2, respectively). Iron is essential for catalyzing enzymatic reactions necessary for numerous cellular processes[55] and iron acquisition is a prerequisite for lymphocyte responses against infection. The protein expression of many of these iron-related genes is mainly controlled through post-transcriptional mechanisms in response to iron levels, whereas the transcriptional regulation of these genes remains less clear[56]. In support of our study, there is evidence that IRF4 directs broad metabolic programming during effector CD8$^+$ T cell differentiation[23]. Thus, our study uncovers a new role for IRF4 in directly regulating a transcriptional network that sustains iron uptake to mediate the adaptive NK cell response, which has not been previously described in innate lymphocyte responses.

The functional cooperation of IRF4 with other transcription factors has previously been described for myeloid cells and adaptive lymphocytes, but not for innate lymphocytes. In B cells, for example, IRF4 can interact with both AP-1 and ETS-related family members, whereas in T cells, IRF4 almost exclusively cooperates with AP-1/ATF family members, including JUN and BATF, which results in recognition of AICE composite motifs[14,44,57,58]. Consistent with the parallel modes of differentiation between NK cells and CD8$^+$ T cells,

our ATAC-seq analysis demonstrates an enrichment of IRF4 and AP-1 motifs during the early adaptive NK cell response, suggesting synergistic cooperation of IRF4 with AP-1 factors in NK cells. Indeed, in this study, we also demonstrate that AP-1 and AICE motifs are among the most enriched motifs in IRF4-bound sites, suggesting that, as in T cells, IRF4 preferentially binds to AP-1 target genes and may directly interact with AP-1 factors to control optimal NK cell antiviral responses[44]. A further understanding of the temporal colocalization and binding of these factors will offer valuable insights into the intricacies of transcriptional regulation by IRF4 in antiviral NK cells.

In addition to expressing IRF4, NK cells also express high levels of IRF8, which shares significant homology with IRF4 and can also synergize with AP-1 factors[59]. Recent studies have demonstrated that IRF4 and IRF8 functions are redundant in the differentiation of dendritic cells[60]; however, our data suggest that the regulation and activity of these two related transcription factors in NK cells are both critical and distinct during viral infection. IRF8 is expressed at high levels in NK cells at steady state and can be further induced by IL-12 + IL-18, whereas the induction of IRF4 requires both activating receptor and proinflammatory cytokine signals, which we found to be conserved between mouse and human. Moreover, we previously showed that deletion of IRF8 in committed NK cells did not affect their development or maturation at steady state, but severely impacted their ability to control MCMV by regulating cellular proliferation[20]. In contrast, here we find a non-redundant and complementary role for IRF4 in controlling the antiviral NK cell response by regulating cell survival and effector differentiation, highlighting distinct functions of these IRF family members. Given that NK cells express both IRF8 and IRF4, it is likely that they have different binding partners and/or bind to distinct genomic regions to control optimal NK cell responses during infection. Thus, the molecular mechanisms underlying the differential regulation of proliferation versus survival by these two related transcription factors drive our quest to uncover the totality of how these IRF family members mediate optimal immune responses.

IRF4 deficiency in humans is rare and often manifests as broad immunodeficiency[22,61,62]. Haploinsufficiency in IRF4 has been reported to result in higher susceptibility to Whipple's disease and dermatitis, whereas a patient with a complete loss of IRF4 developed severe primary immunodeficiency that eventually resulted in multiorgan failure at 2 years of age[22,63]. In this latter IRF4-deficient patient, NK cell number, maturation status and effector functions were largely intact, similar to what we have observed in IRF4-deficient mouse NK cells at steady state. Remarkably, a specific loss of the $NKG2C^{+}CD56^{dim}$ NK cells was observed, compared to healthy pediatric individuals. Although the HCMV serological status of this patient was not reported, the finding suggests that IRF4 may also promote the expansion and differentiation of adaptive $NKG2C^{+}$ NK cells in humans similar to mice. Consistent with such a hypothesis, our study shows that adaptive $NKG2C^{+}$ NK cells express higher levels of IRF4 and are more epigenetically poised to express *IRF4* transcript compared to 'naive' and non-adaptive NK cells. Furthermore, stimulation of human NK cells with the HCMV-derived UL-40-derived peptide along with proinflammatory cytokines resulted in epigenetic remodeling of the *IRF4* promoter to favor accessibility and transcription. Hence, our data together suggest that IRF4 is a critical regulator of the

antiviral NK cell response during CMV infection and its regulation seems to be conserved between mouse and human.

Ultimately, understanding the transcriptional programs that drive optimal NK cell responses to infection can inform our strategies to improve prophylaxis and immunotherapies against emerging infectious diseases such as SARS-CoV-2, but also various cancers. In the context of malignancies, NK cells can accumulate within the tumor microenvironment and play a role in antitumor immunity in addition to controlling metastasis to secondary sites. Indeed, an effector/mature NK cell gene signature has been associated with improved survival in various malignancies[64]; however, in some cancers the tumor-infiltrating NK cells failed to control tumor growth and phenotypic dysfunctions associated with diminished cytotoxic capability and immature NK cell phenotypes were described[65]. Because recently developed NK cell therapies (for example, CIML NK[66,67], NK cell-engagers[68], NK checkpoint blockade[69,70] and chimeric antigen receptor (CAR)-NK cells[71]) have demonstrated promising clinical outcomes for various malignancies, strategies to improve the efficacy of these therapies will be of great value. Current pitfalls in NK cell-based therapies include the relatively short lifespan of in vitro-activated and manipulated NK cells and their sensitivity to immunosuppression in certain tumor microenvironments[72]. Given that IRF4 promotes both effector differentiation and survival of activated NK cells during viral infection, strategies to drive IRF4 expression in NK cells in the tumor microenvironment or in the context of adoptive NK cell-therapy may improve efficacy against cancer. In support of the feasibility of such a strategy, a previous study found that overexpression of BATF (a transcription factor that drives $CD8^+$ T cell effector differentiation) in CAR-T cells counteracted their exhaustion in a preclinical model, an outcome that was dependent on IRF4 (ref. 73).

In summary, our work uncovers a new role for IRF4 in integrating input signals to decouple the innate effector functions of NK cells from their adaptive responses. IRF4 directly controls the adaptive NK cell response by temporally regulating iron uptake that is required for the survival and differentiation of clonally expanding NK cells. Our findings provide additional insight into nutrients and minerals regulating antiviral responses of NK cells. Altogether, we highlight the transcriptional, epigenetic and metabolic requirements underlying a productive NK cell response against infection that may shed light on ways to improve NK cell-based therapeutics.

Online content

Any methods, additional references, Nature Portfolio reporting summaries, source data, extended data, supplementary information, acknowledgements, peer review information; details of author contributions and competing interests; and statements of data and code availability are available at https://doi.org/10.1038/s41590-023-01620-z.

Methods

Mice

All mice used in this study were housed and bred under specific-pathogen-free conditions with food and water in 12-h light–dark cycles at 72 °F with 30–70% humidity at Memorial Sloan Kettering Cancer Center and handled in accordance with the guidelines of the Institutional Animal Care and Use Committee. The following mouse strains were used in this study: C57BL/6 (CD45.2), C57BL/6 CD45.1 (CD45.1)[74], C57BL/6 CD45.1×CD45.2, *Irf4*$^{-/-}$, *Klra8*$^{-/-}$ CD45.1xCD45.2 (Ly49H-deficient)[75] and *Rag2*$^{-/-}$*Il2rg*$^{-/-}$. The *Irf4*$^{-/-}$ mouse strain was a gift from K. Murphy and T. Murphy. Experiments were conducted using 8–10-week-old mice or 8–16 weeks post-transplant mixed bone-marrow chimeric mice and all experiments were conducted using age- and sex-matched mice in accordance with approved institutional protocols.

Virus

MCMV (Smith strain) was serially passaged through BALB/c hosts three times and then salivary gland viral stocks were prepared with a homogenizer for dissociating the salivary glands of infected mice 3 weeks after infection.

Mixed bone-marrow chimeras

Mixed bone-marrow chimeric (mBMC) mice were generated by lethally irradiating (900 cGy) host C57BL/6 CD45.1×CD45.2 animals and reconstituting them with a 1:1 mixture of bone-marrow cells from WT (CD45.1) and *Irf4*$^{-/-}$ (CD45.2) donor mice. Hosts were co-injected with anti-NK1.1 (PK136) to deplete any residual donor and host NK cells. Residual CD45.1^{+}CD45.2^{+} host NK cells were excluded from all analyses.

In vivo adoptive transfer and virus infection

For adoptive co-transfer studies, splenocytes from WT (CD45.1) and *Irf4*$^{-/-}$ (CD45.2) from WT:*Irf4*$^{-/-}$ mBMC mice were mixed to achieve equal numbers of Ly49H^{+}KLRG1^{low} NK cells and injected into Ly49H-deficient recipients 1 day before MCMV infection. Recipient mice in adoptive co-transfer studies were infected either with MCMV by intraperitoneal (i.p.) injection of 1.1×10^3 plaque-forming units (p.f.u.) in 0.5 ml of PBS. For direct infection experiments, WT:*Irf4*$^{-/-}$ mBMC mice were infected with 1.1×10^4 p.f.u. in 0.5 ml PBS. For survival experiments, WT or *Irf4*$^{-/-}$Ly49H^{+} NK cells were sorted from WT:*Irf4*$^{-/-}$ mBMC mice and transferred into *Rag2*$^{-/-}$*Il2rg*$^{-/-}$ mice 1 day before MCMV infection with 4.5×10^3 p.f.u. To measure innate effector function, WT:*Irf4*$^{-/-}$ mBMC mice were directly infected as described and tissues (for example, splenocytes and liver) were collected on day 2 PI. To measure NK cell proliferation, we labeled splenocytes from naive WT:*Irf4*$^{-/-}$ mBMC mice with 5 mM CTV (Thermo Fisher, cat. no. C34557) according to the manufacturer's protocol before transfer into mice and CTV dilution readout was taken on day 3.5–4 PI. For in vivo lymphopenia-driven proliferation assay, splenocytes from WT:*Irf4*$^{-/-}$ mBMC mice were transferred into *Rag2*$^{-/-}$*Il2rg*$^{-/-}$ mice and tissues were collected on day 7 post-transfer.

Isolation of mouse NK cells and flow cytometry

Spleens were dissociated with glass slides and filtered through a 100-μm cell strainer. Flow cytometry and cell sorting were performed on the Cytek Aurora (Cytek Biosciences) and Aria II cytometers (BD Biosciences), respectively. Before cell sorting, NK cells were enriched by incubating whole splenocytes with the following antibodies at 20 μg ml^{-1} against CD3ε (17A2), CD4 (GK1.5), CD8 (2.43), Ter119 (TER-119), CD19 (1D3), Ly6G (1A8) (BioXCell) followed by magnetic depletion using goat anti-rat beads (QIAGEN, cat. no. 310107). For scRNA-seq, enriched splenocytes were then stained with surface markers to identify $Ly49H^+$ NK cells ($CD3/TCRb/CD19^-NK1.1^+CD49b^+Ly49H^+$) and sorted based on congenic markers (CD45.1 and CD45.2) (Extended Data Fig. 7) to identify WT and *Irf4*$^{-/-}$ cells with >95% purity. For in vitro stimulation, total NK cells were defined as $CD3/TCRb/CD19^-NKp46^+CD49b^+$. For intracellular staining, cells were fixed in eBioscience Intracellular Fix & Perm Buffer Set (Thermo Fisher, cat. no. 88–8824-00). For pSTAT5 staining, cells were surface stained, fixed with 2% PFA for 10 min at 37 °C, washed twice with PBS and incubated with pre-chilled BDPhosFlowIII (BD Biosciences, cat. no. 558050) at 4 °C for 30 min before staining with 1:50 dilution of pSTAT5 antibody. A list of antibodies used for flow cytometric analysis can be found in Supplementary Table 1.

In vitro receptor and cytokine stimulations

High-binding 96-well flat-bottom plates were coated with 100 μl per well of 20 μg ml^{-1} anti-NK1.1 (Clone PK136, BioLegend, cat. no. 108759) or anti-Ly49H (Clone 3D10, BioLegend, cat. no. 144718) in PBS at 4 °C overnight. The next day, splenic NK cells were sorted as described and sorted cells were resuspended in complete RPMI (10% FBS, 1× L-glutamine, 1× sodium pyruvate, 1× BME, 1× MEM-NAA and 25 mM HEPES). For cytokine stimulations, we used 20 ng ml^{-1} mouse IL-2 (Peprotech, cat. no. 210–21), 20 ng ml^{-1} mouse IL-15 (Peprotech, cat. no. 210–15), 20 ng ml^{-1} mouse IL-12 (R&D Systems, cat. no. 419-ML-050), 10 ng ml^{-1} mouse IL-18 (MBL, cat. no. B002–5) and/or 100 IU mouse IFN-α (R&D Systems, cat. no. 12105–1). For the unstimulated condition or anti-NK1.1 alone, 5 ng ml^{-1} IL-15 was added into the medium to prevent cell death. Then, 50,000 cells were plated per well for each indicated condition overnight. To assess effector functions, 2 million splenocytes were plated in 96-well U-bottom plates and stimulated with 10 ng ml^{-1} and 1 μg ml^{-1} PMA (MiliporeSigma, cat. no. P8139–1MG) and ionomycin (MiliporeSigma, cat. no. I0634–1MG), respectively.

Ex vivo cell death assay

Spleens from MCMV-infected WT:*Irf4*$^{-/-}$ mBMC mice were taken 5 d PI and resuspended in PBS and plated in 96-well U-bottom plates at 2 million cells per well. Plated splenocytes were then treated with the indicated concentrations of BCL2 inhibitor, ABT199 (also known as venetoclax) (MedChemExpress, cat. no. HY-15531) in the presence of CaspGLOW Fluorescein Active Caspase Staining kit (Thermo Fisher, cat. no. 88–7003-42) per manufacturer's protocol for 90 min at 37 °C. Cells then were washed with FACS buffer and stained with surface antibodies before sample collection by flow cytometry.

Mouse single-cell RNA-sequencing and analysis

Ly49H$^+$ NK cells (CD3/TCRb/CD19$^-$NK1.1$^+$CD49b$^+$Ly49H$^+$) from either WT or *Irf4*$^{-/-}$ NK cells were sorted from spleens of MCMV-infected WT:*Irf4*$^{-/-}$ mBMC mice as described from day 0, 2, 4 and 7 PI and stained with barcoded antibodies (Total-Seq B, BioLegend; Supplementary Table 1)[76]. After hash-staining, WT and *Irf4*$^{-/-}$Ly49H$^+$ NK cells were mixed at a 1:1 ratio for each time point. The single-cell RNA-seq from these pooled FACS-sorted cell suspensions was then performed on Chromium instrument (10x Genomics) following the user guide manual for 3′ v.3.1. In brief, FACS-sorted cells were washed once with PBS containing 1% bovine serum albumin (BSA) and resuspended in PBS containing 1% BSA to a final concentration of 700–1,300 cells per μl. The viability of cells was above 80%, as confirmed with 0.2% (w/v) Trypan blue staining (Countess II). Cells were captured in droplets. Following reverse transcription and cell barcoding in droplets, emulsions were broken and cDNA-purified using Dynabeads MyOne SILANE (Thermo Fisher, cat. no. 37002D) followed by PCR amplification as per the manual instructions. Samples were multiplexed together on one lane of 10x Chromium (using Hash Tag Oligonucleotides (HTOs)) following a previously published protocol[76]. Final libraries were sequenced on Illumina NovaSeq S4 platform (R1, 28 cycles; i7, 8 cycles; and R2, 90 cycles). The cell–gene count matrix was constructed using the Sequence Quality Control package (https://github.com/dpeerlab/seqc)[77]. Viable cells were identified on the basis of library size and complexity, whereas cells with >20% of transcripts derived from mitochondria were excluded from further analysis. After mitochondrial and doublet cleanup, the raw count matrix was normalized by median library size normalization followed by log transformation. The Louvain algorithm with $k = 30$ was used to perform clustering and Euclidean distance was used as the metric to construct a nearest-neighbor graph[78]. PAGA analysis was performed as described using scanpy (https://github.com/theislab/paga)[79,80]. MAST was then used to perform differential expression (DE) analysis between hash-ed samples, and GSEA (https://github.com/zqfang/GSEApy) was then performed on DE genes (FDR < 0.05 and |coef| > 0) using ‘MSigDB_Hallmark_2020’ gene set and significant pathways were identified based on $P_{adj} < 0.05$ (refs. 31,81). In some cases, MAGIC was used to impute transcript counts[82]. MPEC and SLEC signatures were obtained from GEO under accession code GSE8678 (ref. 83).

Mouse bulk RNA-seq and ATAC-seq analyses

Analysis of RNA-seq and ATAC-seq for the MCMV time course was performed from a previously published dataset (GEO SuperSeries accession code GSE106139). For bulk ATAC-seq data generated in this study, peak calling and atlas generation were described previously[1]. For this dataset, reproducible peaks showing an irreproducible discovery rate value of 0.05 or less in at least one replicate pair were retained. A union of both inclusively merged overlapping peaks and unique reproducible peaks for each condition was used to generate the final atlas and was used for further analysis. Motif analysis was performed on differentially accessible regions with high fold change ($\log_2FC \geq 1$, $P_{adj} < 0.05$) by HOMER[84].

IRF4 chromatin immunoprecipitation by sequencing

Splenic WT NK cells ($NK1.1^{+}CD49b^{+}$) were expanded ex vivo for 2 weeks in complete IMDM (10% FBS, 1% pen/strep, 1× BME, 1× MEM-NAA, 1× HEPES) in the presence of 50 ng ml^{-1} of human IL-15 (Miltenyi, cat. no. 130–095-766). Then, 10 million IL-15 expanded NK cells were then stimulated with anti-NK1.1 + cytokines (IFN-α + IL-12/18 + IL-2/15) (see concentrations above) or left unstimulated in 5 ng ml^{-1} of hIL-15 overnight in a six-well plate. Upon stimulation, cells were then washed with 1× PBS and crosslinked by slowly adding 16% formaldehyde to a final concentration of 1% formaldehyde, agitated and incubated for 10 min at room temperature (RT). Glycine was then added to quench the sample and incubated at RT for 5 min and on ice for 15 min. Cells were then centrifuged and 600 µl cell lysis buffer (50 mM HEPES-KOH, 140 mM NaCl, 1 mM EDTA, 10% glycerol, 0.5% NP-40 and 0.25% Triton-X-100) was added into cell pellets and incubated for 4 min on ice, spun at 600*g* for 10 min at 4 °C and supernatant was discarded. Then, 600 µl of nuclei wash buffer (10 mM Tris-Cl, pH 8.0, 200 mM NaCl, 1 mM EDTA and 0.5 mM EGTA) was added to each sample and resuspended gently, spun at 600*g* for 10 min at 4 °C and the supernatant was discarded. Cell pellets were then resuspended with nuclei lysis buffer and incubated for 5 min on ice and sonicated for eight cycles, 30 s on and 30 s off high at 4 °C. Upon sonication, Triton-X-100 was added to a final concentration of 1%. Nuclei were centrifuged for 20 min at 18,500*g* at 4 °C and the supernatant was transferred into a new tube where 10% of samples were then aliquoted into a new tube as ‘input’. Then, 25 µl Protein A (Thermo Scientific, cat. no. 21181) was added into each sample and agitated for 30 min at 4 °C on a rotator. Moreover, protein A beads (Thermo Scientific, cat. no. 88845) were blocked with ice-cold RIPA buffer by adding BSA to a final concentration of 0.1% and agitated for 3 min at 4 °C on a rotator. Upon incubation, immunoprecipitated samples were centrifuged for 30 s for 4 °C at 2,400*g* and supernatant was transferred into new tubes and combined with blocked protein A beads. Anti-IRF4 (clone D9P5H, Cell Signaling, cat. no. 15106S) was added gently to prevent bead shearing and incubated on a rotator overnight at 4 °C. Samples were then centrifuged at 2,400*g* for 1 min at 4 °C and supernatant was removed gently. Beads were then washed twice with RIPA buffer, four times with ChIP wash buffer (100 mM Tris-Cl, pH 8.5, 500 mM LiCl, 1% NP-40 and 1% sodium deoxycholate), twice again with RIPA buffer and twice with ChIP TE buffer (10 mM Tris, pH 7.5, 1 mM EDTA and 50 mM NaCl). Beads were centrifuged at 2,400*g* for 1 min at 4 °C between all washes and supernatant was removed after the last wash. Then, 100 µl of decrosslinking buffer (TE buffer, 0.5% SDS buffer and 1× Proteinase K) was added into every sample and incubated for 2 h at 55 °C. After incubation, samples were vortexed and then transferred to 65 °C and incubated overnight. Samples were then centrifuged at 2,400*g* for 1 min at RT, transferred into new tubes and purified using QIAGEN PCR purification kit (QIAGEN, cat. no. 28104). Immunoprecipitated DNA was quantified by PicoGreen and the size was evaluated by Agilent BioAnalyzer. Illumina sequencing libraries were prepared using the KAPA HTP Library Preparation kit (Kapa Biosystems, cat. no. KK8234) according to the manufacturer’s instructions with up to 5 ng input DNA and 8–12 cycles of PCR. Barcoded libraries were run on the NovaSeq 6000 in a PE100 run, using the NovaSeq 6000 S4 Reagent kit (200 Cycles) (Illumina). An average of 29 million paired reads were generated per sample.

IRF4 ChIP-seq analysis

Paired reads were trimmed for adaptors and subjected for removal of low-quality reads using Trimmomatic (v.0.39) and aligned to the mm10 reference genome using Bowtie2 (v.2.4.1). Upon alignment, peaks were called using MACS2 (v.2.2.7.1) with input samples using narrow peak parameters '–q 0.05 –B –SPMR'. Peaks were annotated using 'ChIPpeakAnno' package with the UCSC mm10 reference genome model[85,86]. IRF4-binding signal was plotted using 'plotHeatmap' function of deepTools[87]. Motif enrichment analysis was conducted using HOMER algorithm (HOMER v.4.10) using IRF4 atlas found in the stimulated condition with parameter '–size given –len 6,8,10,12,15 –mset vertebrates –mast' for de novo motif analysis.

Integration of IRF4 ChIP-seq, bulk RNA-seq and ATAC-seq

To assess the relationship between IRF4-bound regions, AP-1/AICE/IRF4 motifs, chromatin accessibility and gene expression during MCMV time course, we first scanned the mm10 genome for AP-1/AICE/IRF4 motifs using HOMER 'scanMotifGenomeWide.pl' function and overlapped these motifs map with ATAC-seq atlas from Ly49H$^+$ NK cells during an MCMV time course to exclude any irrelevant motifs[84]. We further filtered this atlas by overlapping it with our IRF4 ChIP-seq data. Using this final atlas, we plotted the median of normalized counts from ATAC-seq data at each time point. Using the method above, we looked at the expression of IRF4-bound AICE motif-containing genes during MCMV infection that were differentially expressed at any point during the infection. We then created a customized pathway using 'fgsea' package (https://github.com/ctlab/fgsea) based on DEGs from our scRNA-seq dataset that were either enriched in WT or *Irf4*$^{-/-}$Ly49H$^+$ NK cells at any time point and used the 'geseca' function to perform GSEA with 'minSize = 20, maxSize = 500, and center = FALSE' parameters.

Kynurenine uptake assay

Two million splenocytes from day 5 MCMV-infected WT:*Irf4*$^{-/-}$ mBMC mice were isolated and stained with antibodies against surface markers. After staining, cells were washed, resuspended in 37 °C prewarmed HBSS++ and plated in a 96-well U-bottom plate. Kynurenine (Selleckchem, cat. no. S5839) (200 μM), kynurenine + lysine (MiliporeSigma, cat. no. L8662–25G) (200 μM + 5 mM), kynurenine + leucine (MiliporeSigma, cat. no. L8912–25G) (200 μM + 5 mM) were added into the wells and incubated for 5 min at 37 °C. After 5 min, cells were immediately fixed in 1% PFA for 30 min at RT in the dark, washed with FACS buffer and kynurenine fluorescence was read by Cytek Aurora.

Transferrin uptake assay

A transferrin uptake assay was performed as described with slight modifications[54]. Briefly, 2 million splenocytes from day-5 MCMV-infected mBMC mice were isolated and resuspended in serum-free RPMI + 0.5% BSA and plated in a 96-well U-bottom plate. Cells were then treated with or without 5 μg ml^{-1} of fluorescein-conjugated transferrin (Thermo Fisher, cat. no. T2871) for 10 min at 37 °C. The reaction was stopped as described and stained for surface markers before fixation with BD CytoFix/Cytoperm kit (BD Biosciences, cat. no. 554714).

In vivo pharmacological treatment

WT mice were directly infected with MCMV and were i.p. treated with either PBS, BCH, a LAT1 inhibitor (MedChemExpress, cat. no. HY-108540) or deferiprone, an iron chelator (Selleckchem, cat. no. S4067), at 200 mg kg^{-1} every day from day 2 to day 4 PI. On day 5, mice were collected and analyzed for NK cell expansion and differentiation.

Human bulk RNA-seq

Bulk NK cell subset RNA-seq dataset was taken from a deposited dataset under EGA EGAS00001005025 (ref. 27). IRF4 expression was plotted as $\log_2$ FPKM. A bulk RNA-seq count matrix of $NKG2C^+$ NK cells stimulated with control or UL-40 peptide + IL-12/18 was taken from a previously published dataset (GEO accession code GSE109823) and differential expression analysis was performed using DESeq2 (v.1.34)[88,89].

Human single-cell ATAC-sequencing analysis

scATAC-seq datasets were generated by Rückert et al. (GEO SuperSeries accession code GSE197037) and the detailed methodology can be found in the original manuscript. Codes for analyses are available at https://github.com/timorueckert/Clonal_NK. Briefly, scATAC-seq reads were mapped with CellRanger-ATAC count to the GRCh38 reference genome, hardmasked for regions that would otherwise interfere with mapping to the mitochondrial genome[90] to generate count tables and fragments files that were used for further analysis. Peak sets called from different experiments were reduced to a joint atlas as a basis for combined analysis of individual experiments using Signac[91]. Cells were then filtered for outliers based on nucleosome signal (<1–1.2), transcription start site enrichment (>2.5–4) and the frequency of reads in peaks (>55–70%) and blacklisted regions (<0.0001). Antibody-derived tag (ADT) and HTO counts were imported, centered-log-ratio normalized and joined with the scATAC-seq data. Normalized hashtag reads were used for doublet exclusion and to demultiplex donors. Chromatin accessibility counts were normalized by term frequency-inverse document frequency (TF-IDF), data from different experiments were merged and dimensionality was reduced by singular value decomposition. The resultant latent semantic index (LSI) was integrated across experiments using Harmony[92] and used as input into further dimensionality reduction by UMAP and neighborhood graph-based clustering. A small population of non-NK cells based on their lack of CD56 and CD16 expression and high levels of CD127 and CD117 were excluded from analysis. The merged and integrated dataset was used for peak calling using MACS2 (ref. 86) to enable more-sensitive calling of cluster-specific open chromatin regions. This new assay was again processed by LSI, followed by anchor-based integration of donors[93]. The UMAP embeddings and clustering for final analysis were based on this integrated LSI. Unbiased clustering initially yielded three major clusters that were annotated based on surface protein expression, with early $CD56^{dim}$ NK cells separated from $CD56^{bright}$ NK cells by further sub-clustering. For the in vitro-activated cells, quality control, joining of ADT, HTO and scATAC-seq counts, demultiplexing, peak calling on the full dataset with MACS2, normalization and dimensionality reduction by LSI were performed as described above. The two analyzed donors were integrated with Harmony and the corrected LSI was used for UMAP embedding and clustering. Upon inspection of the distribution of cells from

the different conditions and donors, the majority of cells were clearly separated based on whether they had received peptide or cytokine stimulation, but we also noted two smaller clusters, each enriched for cells from one donor respectively, in which cells from different conditions were mixed, likely driven by underlying donor-specific signatures that were not corrected by Harmony integration. To analyze stimulus-induced changes in chromatin accessibility, we focused the analysis on the majority of cells that clustered by conditions and irrespective of donor origin. After clustering these cells at higher resolution, we annotated clusters according to a clear enrichment of cells derived from different conditions.

Human NK cell stimulation

Peripheral blood samples were collected from healthy human donors following approval from the Memorial Sloan Kettering Cancer Center Institutional Review Board and donors provided informed, written consent. Buffy coats were obtained from healthy volunteer donors via the New York Blood Center (http://nybloodcenter.org/). The Memorial Sloan Kettering Cancer Center Institutional Review Board waived the need for additional research consent for anonymous New York Blood Center samples. Peripheral blood mononuclear cells (PBMCs) from each donor were isolated by Ficoll density gradient centrifugation and cryopreserved in FBS with 10% dimethylsulfoxide. Frozen PBMCs were thawed and rested for 6 h in complete RPMI-1640 medium (10% heat-inactivated FBS, 100 U ml^{-1} penicillin and 100 μg ml^{-1} streptomycin) and incubated at 37 °C with 5% CO_2. In a 96-well U-bottom plate, PBMCs (4×10^5 cells per well) were incubated overnight in 200 μl complete RPMI with or without IL-12 at 10 ng ml^{-1} (BioLegend, cat. no. 573004) and IL-18 at 50 ng ml^{-1} (InvivoGen, cat. no. rcyec-hil18). The following day, 50 μl medium was removed in each well and HLA class I negative K562 (1:4 ratio, ATCC, cat. no. CCL-243) or complete RPMI was added in the presence of anti-CD107a (1:100 dilution, BD Biosciences, cat. no. 554724). After 1.5 h of co-culture, 10 μg ml^{-1} Brefeldin A (MP Biomedicals, cat. no. 02159027-CF) and 1× Golgi stop (BD Biosciences, cat. no. 554724) were added to each well and incubated for another 3.5 h. The cells were then washed with PBS and stained with Live/Dead (Invitrogen, cat. no. L34957) for 20 min at RT. Cells were then washed with FACS buffer and cell surface staining was performed at RT for 30 mins. The cells were then fixed and permeabilized with the eBioscience kit (Thermo Fisher, cat. no. 88–8824-00) according to the manufacturer's recommendations. Intracellular staining was incubated for 25 min at RT. CD107a and IFN-γ production were used to determine NK cell activation.

Reporting summary

Further information on research design is available in the Nature Portfolio Reporting Summary linked to this article.

Extended Data

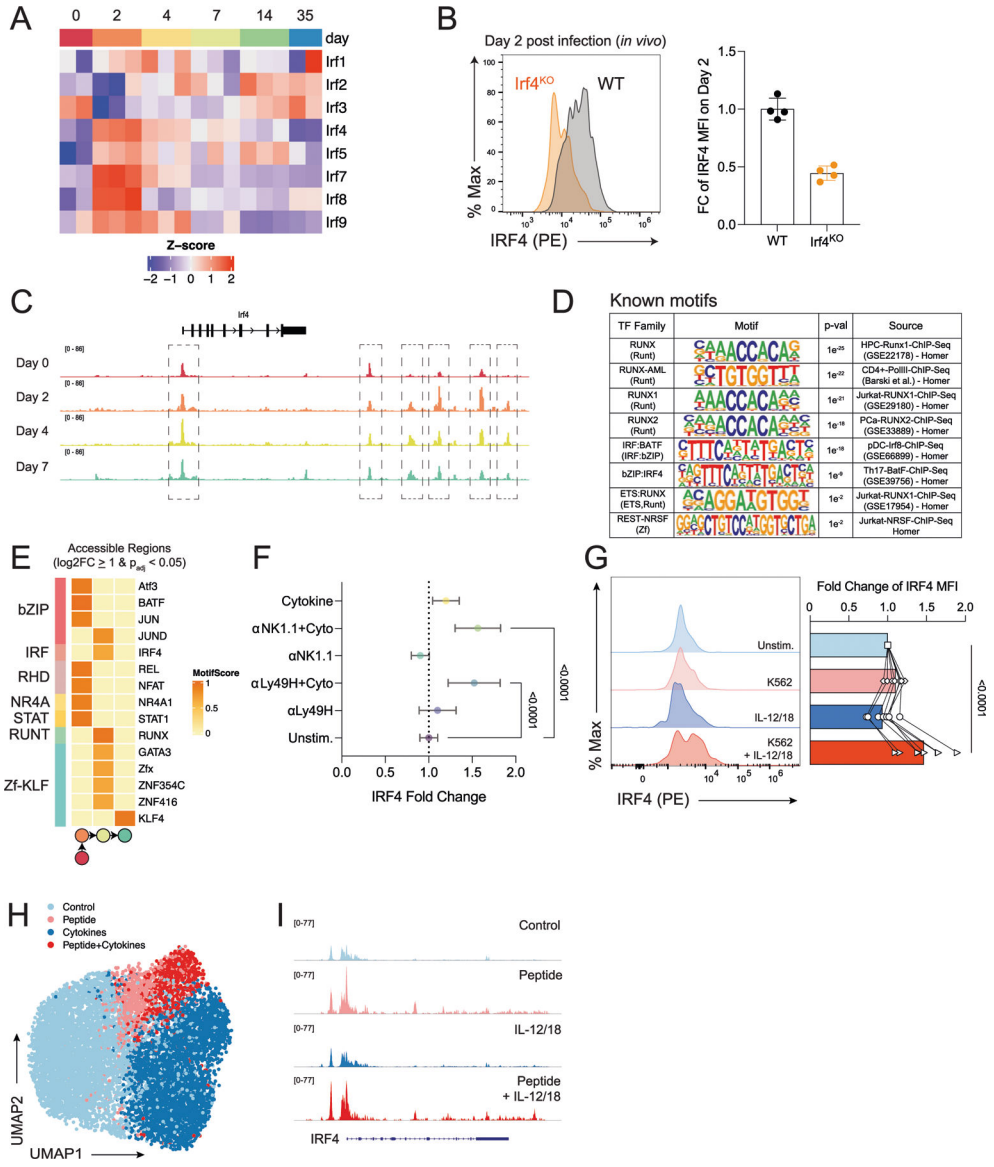

Extended Data Fig. 1 |. Evidence of IRF4-mediated transcriptional control in NK cells.

a. Heatmap of IRF family members expression in NK cells throughout the course of MCMV infection represented as z-score of $\log_2$ normalized counts based on RNA-seq. **b**. Representative histogram of IRF4 expression in WT and *Irf4*$^{-/-}$ NK cells on day 2 PI (n = 4 biological replicates). **c**. Tracks (top) show chromatin accessibility dynamics of the *Irf4* locus in Ly49H$^+$ NK cells at days 0, 2, 4, and 7 PI as assessed by ATAC-seq. Graphs (bottom) show normalized counts for each peak indicated. **d**. Tables of enriched known motifs of highly accessible regions ($\log_2$FC > 1 & p_{adj} < 0.05) on day 4 PI versus day 2 PI from ATAC-seq data of Ly49H$^+$ NK cells after MCMV infection. **e**. Heatmap of motif score from *de novo* motif analysis on highly accessible regions ($\log_2$FC > 1 & p_{adj} < 0.05) during day 0, 2, 4, and 7 transition based on ATAC-seq data of Ly49H$^+$ NK cells after MCMV infection. **f**. IRF4 expression of sorted naïve splenic NK cells after

an overnight stimulation with the indicated stimuli. IRF4 induction is displayed as fold change of IRF4 MFI over unstimulated condition (n = 6 biological replicates per condition). Two-way ANOVA test adjusted for multiple comparisons was used for statistical analysis. **g**. Representative histogram of IRF4 expression upon indicated stimulation gated on human CD56^{bright} NK cells. Data are presented as paired fold change of IRF4 MFI compared to unstimulated condition (n = 8 donors per condition). Two-way ANOVA test adjusted for multiple comparisons was used for statistical analysis. **h**. UMAP embedding of scATAC-seq data from *in vitro* stimulated human NK cells (sorted on CD3^{-}CD14^{-}CD19^{-}CD7^{+}NKG2C^{+}) from HCMV^{-} donors. **i**. Coverage plot of the *IRF4* locus from *in vitro* stimulated human NK cells as in (H).

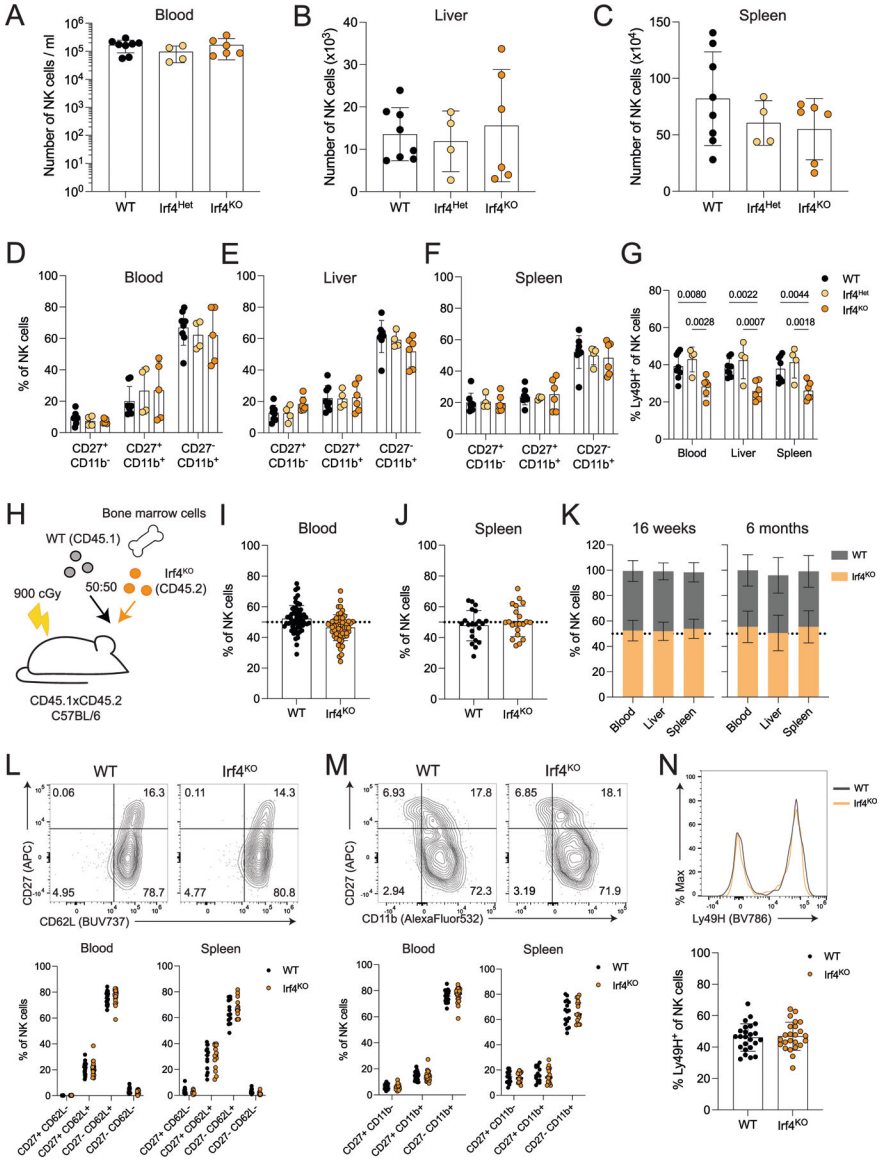

Extended Data Fig. 2 |. IRF4 is dispensable for NK cell development and homeostasis.

a–c. Number of NK cells in blood (A), liver (B), and spleen (C) of WT (n = 8), *Irf4*$^{+/-}$ (n = 4), or *Irf4*$^{-/-}$ (n = 6) mice at 8 weeks old. **d–f**. Maturation status based on the expression of CD27 and CD11b of WT (n = 8), *Irf4*$^{+/-}$ (n = 4), or *Irf4*$^{-/-}$ (n = 5 for blood, and n = 6 for liver and spleen) mice in the blood (D), liver (E), and spleen (F) at 8 weeks old. **g**. Percentage of Ly49H^{+} NK cells within NK cells (Lineage-NK1.1+ CD49b+) of WT (n = 8), *Irf4*$^{+/-}$ (n = 4), or *Irf4*$^{-/-}$ (n = 6) mice at 8 weeks old. **h**. Experimental schematic of WT:*Irf4*$^{-/-}$ mixed bone-marrow chimera (mBMC) generation. **i–k**. Percentage of NK cells of WT or *Irf4*$^{-/-}$ mice from WT:*Irf4*$^{-/-}$ mBMC in the blood (n = 60 biological replicates) (I) and spleen (n = 21 biological replicates) (J) after 8 weeks (I-J), 16 weeks (n = 3 biological replicates) or 6 months (n = 5 biological replicates) post-transplant (K). **l**. Representative of flow plots of CD62L versus CD27 of either WT or *Irf4*$^{-/-}$ NK cells from WT:*Irf4*$^{-/-}$ mBMC in the blood and spleen 8 weeks post-transplant. Data are represented as percentage of each subset within total NK cells of each genotype (n = 22 biological replicates in blood, and n = 13 biological replicates in spleen). **m**. Representative of flow plots of CD11b versus CD27 of either WT or *Irf4*$^{-/-}$ NK cells from WT:*Irf4*$^{-/-}$ mBMC in the blood and spleen 8 weeks post-transplant. Data are represented as percentage of each subset within total NK cells of each genotype (n = 22 biological replicates in blood, and n = 16 biological replicates in spleen). **n**. Histogram and percentage quantification of Ly49H^{+} NK cells within splenic NK cells of either WT or *Irf4*$^{-/-}$ NK cells from WT:*Irf4*$^{-/-}$ mBMC (n = 24 biological replicates). Data are represented as mean ± SEM and are representative of or pooled from at least two independent experiments. Unpaired (A-G) and paired (I-N) two-tailed t-tests were performed.

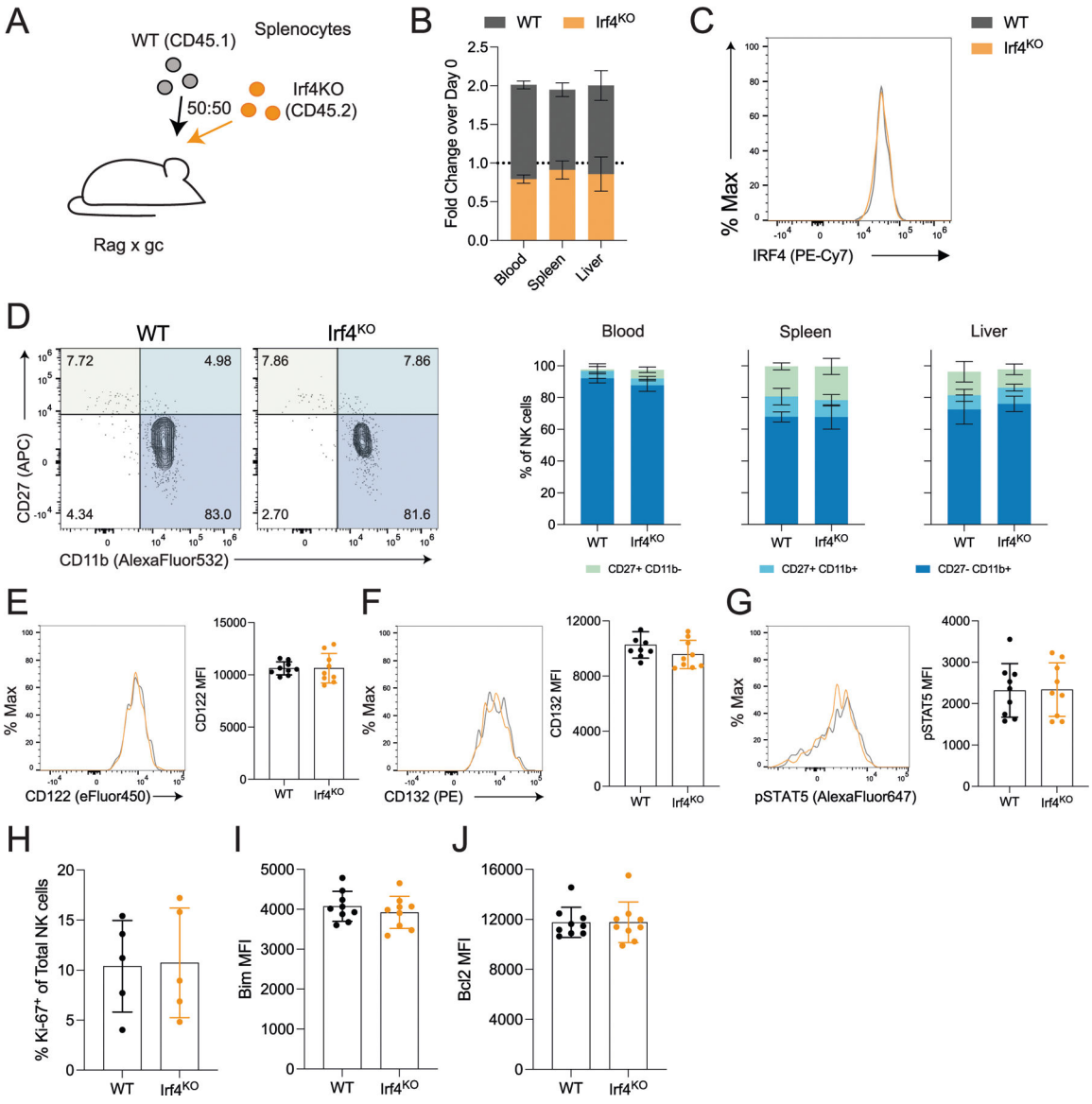

Extended Data Fig. 3 |. IRF4 is not required for lymphopenia-driven proliferation and differentiation.

a. Experimental schematic of adoptive transfer of WT and *Irf4*$^{-/-}$ NK cells into *Rag2*$^{-/-}$ *Il2rg*$^{-/-}$ mice. **b**. Fold change chimerism between WT and *Irf4*$^{-/-}$ NK cells on day 7 over day 0 (pre-transfer) in blood, liver, and spleen (n = 3 biological replicates in blood, and n = 6 biological replicates in liver and spleen). **c**. Representative histogram of IRF4 expression between transferred WT and *Irf4*$^{-/-}$ NK cells on day 7 post-transfer into *Rag2*$^{-/-}$ *Il2rg*$^{-/-}$. **d**. Representative flow plots of CD27 and CD11b expression between WT and *Irf4*$^{-/-}$ NK cells on day 7 post-transfer. Data are represented as percentage of each subset within WT or *Irf4*$^{-/-}$ NK cells in indicated tissues (n = 3 biological replicates). **e**. Histogram of CD122 and quantification of CD122 MFI between WT and *Irf4*$^{-/-}$ NK cells on day 7 post-transfer in the spleen (n = 9 biological replicates). **f**. Histogram of CD132 and quantification of CD132 MFI between WT and *Irf4*$^{-/-}$ NK cells on day 7 post-transfer in the spleen (n = 9 biological replicates). **g**. Histogram of pSTAT5 and quantification of pSTAT5 MFI between WT and

Irf4$^{-/-}$ NK cells on day 7 post-transfer in the spleen (n = 9 biological replicates). H-J. **h–j**. Quantification of Ki-67 staining in the blood and spleen between WT and *Irf4*$^{-/-}$ NK cells (H, n = 5 biological replicates per group), BIM and BCL2 MFI from splenic NK cells (I-J, n = 9 biological replicates). Data are represented as mean ± SEM and are representative of or pooled from at least two independent experiments. Paired two-tailed t-test was performed unless stated otherwise.

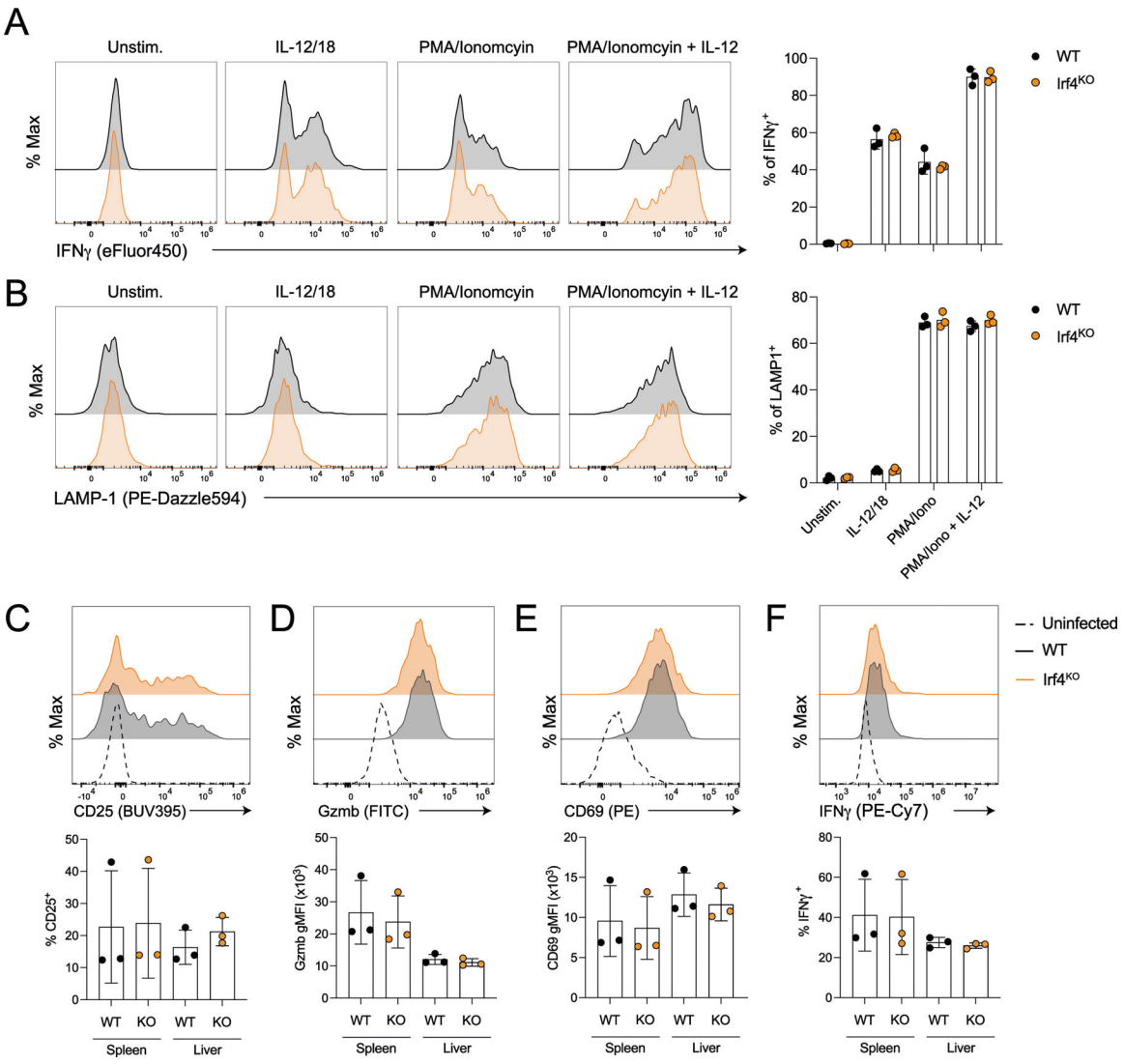

Extended Data Fig. 4 |. IRF4-deficient NK cells have intact effector functions.

a, **b** Representative histograms and quantification of IFN-γ production (A) and LAMP-1 (also known as CD107a) (B) from either naive WT (gray) or *Irf4*$^{-/-}$ (orange) NK cells upon *in vitro* stimulation with nothing, IL-12 + IL-18, PMA + Ionomycin, or PMA + Ionomycin + IL-12 for 3 hours. **c–f**. Representative histograms (upper panels) and quantifications (bottom panels) of CD25, Gzmb, CD69, and IFN-γ expression gated on Ly49H^{+} NK cells from MCMV-infected WT:*Irf4*$^{-/-}$ mBMC on day 2 PI. Data are represented as mean ± SEM and

are representative of or pooled from at least two independent experiments. n = 3 biological replicates per group. Paired two-tailed t-test was performed unless stated otherwise.

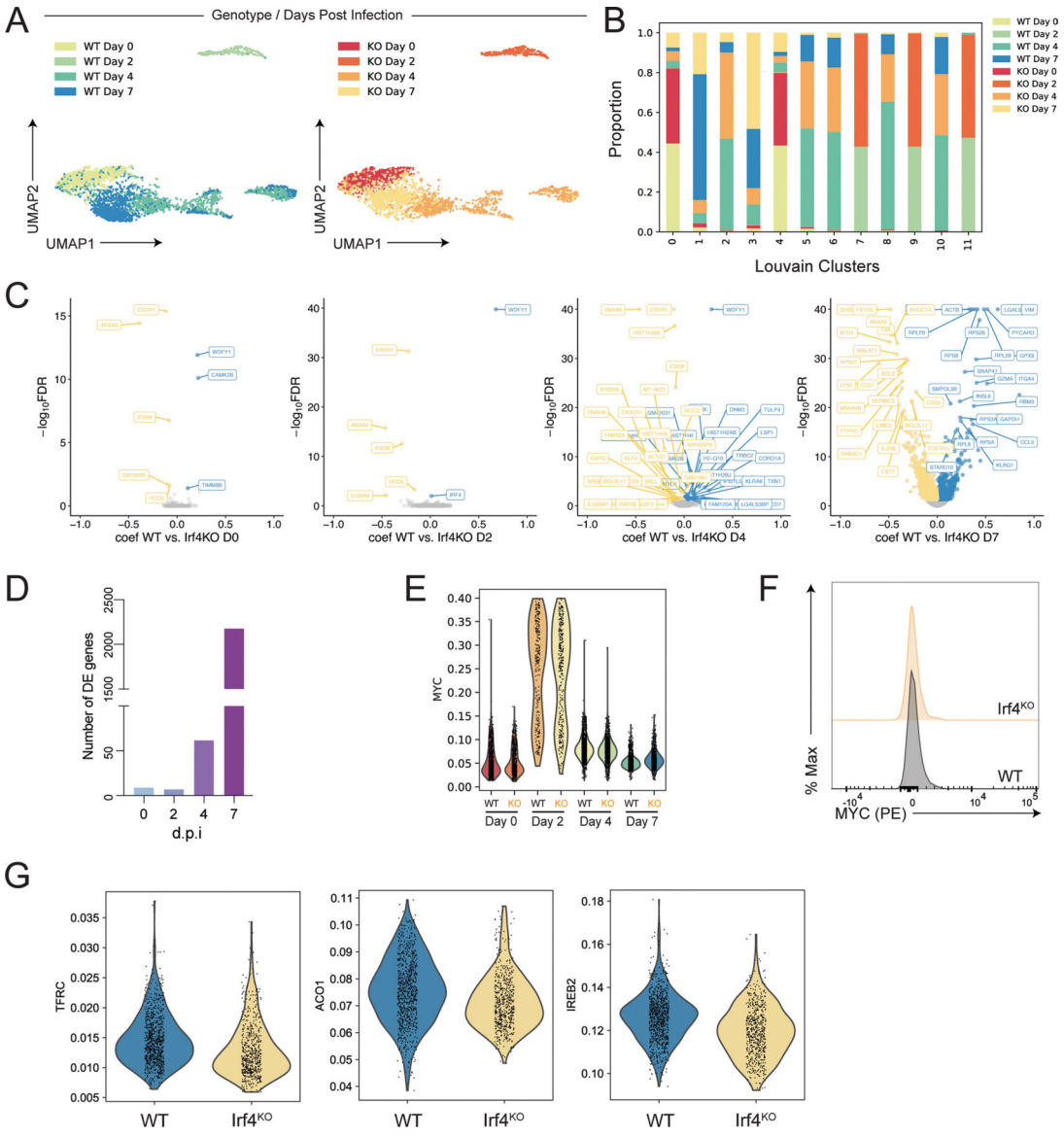

Extended Data Fig. 5 |. scRNA-seq Analysis of wild-type versus IRF4-deficient NK cells.

a. UMAP embedding of WT (left) or *Irf4*$^{-/-}$ (right) of Ly49H^{+} NK cells colored by genotypes and days post-infection. **b**. Proportion of each genotype from each time points per Louvain clusters. **c**. Volcano plot of scRNA-seq as determined by MAST between WT and *Irf4*$^{-/-}$ Ly49H^{+} NK cells on day 0, 2, 4 and 7 PI. Blue and yellow points represent significant genes (FDR < 0.05) that are upregulated in WT or *Irf4*$^{-/-}$ Ly49H^{+} NK cells, respectively. **d**. Number of differentially expressed genes between WT or *Irf4*$^{-/-}$ Ly49H^{+} NK cells from each time point as identified by MAST. **e**. Violin plot quantification of normalized reads for MYC transcript by scRNA-seq between WT and *Irf4*$^{-/-}$ Ly49H^{+} NK cells. **f**. Representative histogram of Myc protein by flow cytometry between WT (gray)

and *Irf4*$^{-/-}$ (orange) Ly49H^{+} NK cells on day 5 PI. **g**. Violin plot quantification of MAGIC-imputed reads for CD71 (*Tfrc*), IRP1 (*Aco1*), and IRP2 (*Ireb2*) on day 7 PI between WT (blue) and *Irf4*$^{-/-}$ (yellow) Ly49H^{+} NK cells by scRNA-seq.

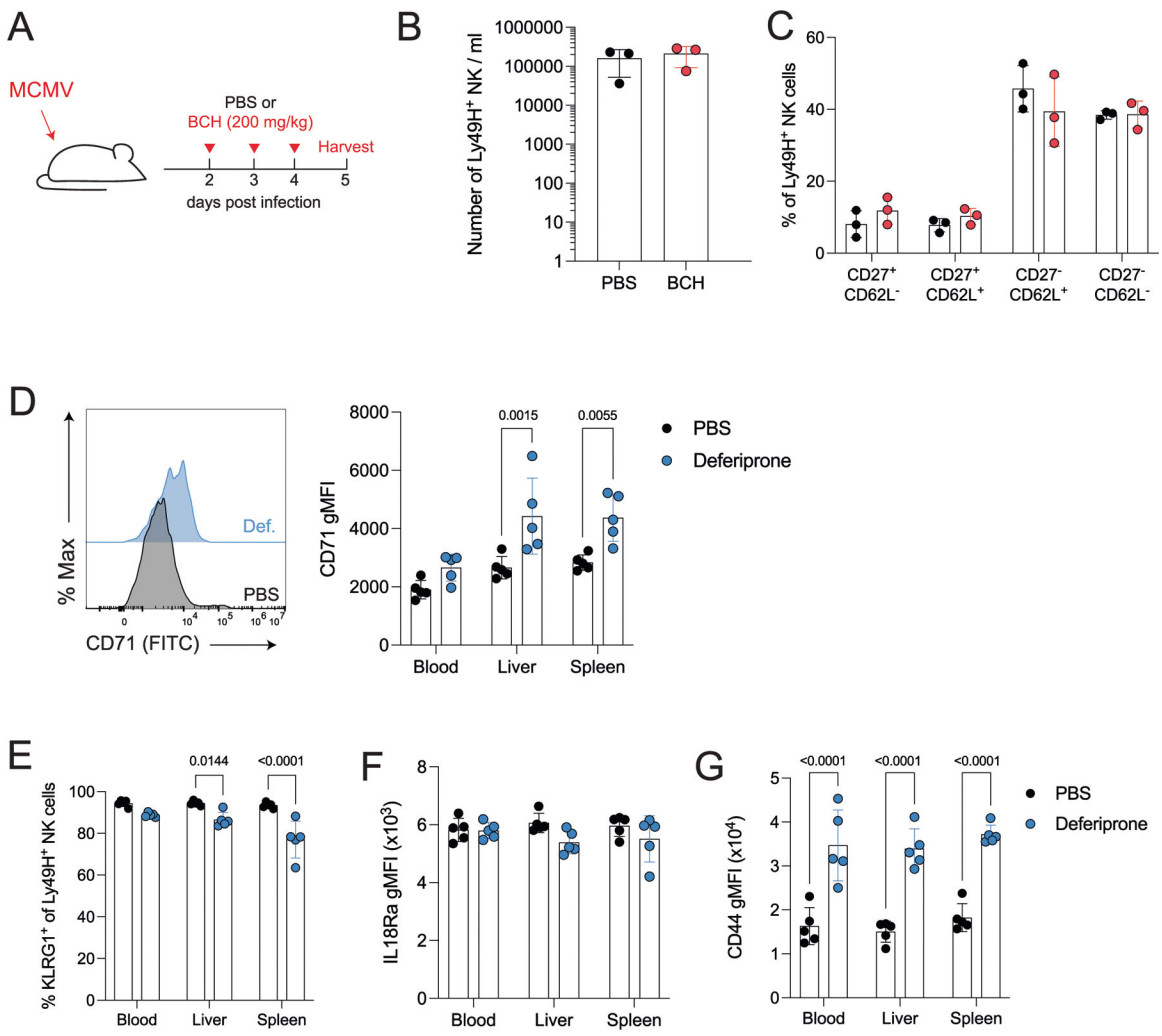

Extended Data Fig. 6 |. Nutrient requirements for adaptive NK cell response.

a. Experimental schematic of PBS or BCH treatment upon MCMV infection in WT mice. **b**. Quantification of Ly49H^{+} NK cell numbers of MCMV-infected mice treated with PBS or BCH on day 5 PI from blood (n = 3 biological replicates per group). **c**. Percent of CD62L versus CD27 subsets on day 5 PI of PBS- (black) or BCH-treated (red) mice (n = 3 biological replicates per group). **d**. Representative histogram and gMFI of CD71 expression on Ly49H^{+} NK cells on day 5 PI in PBS or Deferiprone-treated mice. Upregulation of CD71 was used as a readout for successful iron chelation (n = 5 biological replicates per group). **a–g**. Percent of KLRG1^{+} Ly49H^{+} NK cells (E), and gMFIs of IL18Ra (F) and CD44 (G) on Ly49H^{+} NK cells on day 5 PI from PBS or Deferiprone-treated mice (n = 5 biological replicates per group). Data are represented as mean ± SEM and are representative of at least two independent experiments. Two-way ANOVA adjusted for multiple comparisons was performed unless stated otherwise.

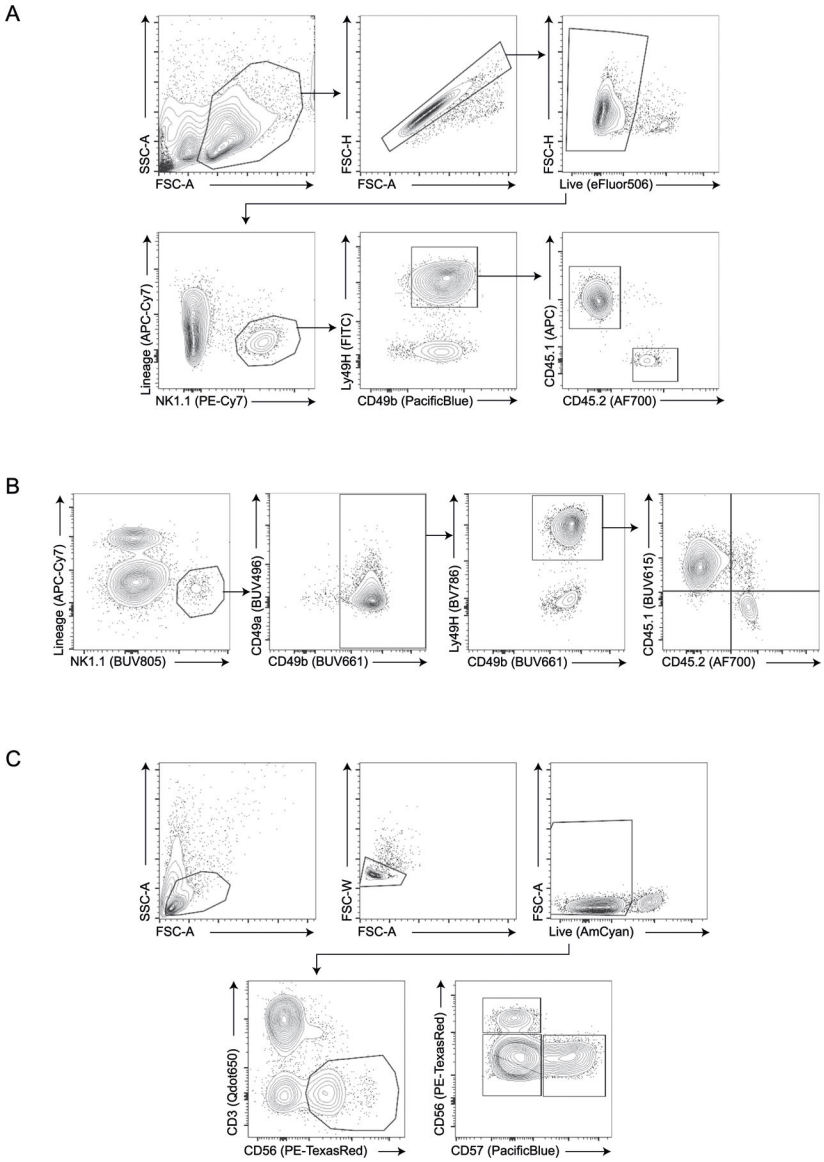

Extended Data Fig. 7 |. Gating strategies to identify NK cells.

a. Gating strategy for sorting WT or *Irf4*$^{-/-}$ Ly49H^{+} NK cells. **b**. Gating strategy for phenotypic analysis of Ly49H^{+} NK cells after lymphocytes, singlets and live cells cleanup (as depicted in Extended Data Fig. 7a). **c**. Gating strategy for human NK cells.

Supplementary Material

Refer to Web version on PubMed Central for supplementary material.

Acknowledgements

We thank members of the Sun laboratory, K. Lupo and X. Chen, as well as the Single-Cell Analytics Innovation Lab at the Sloan Kettering Institute for technical support and experimental assistance, especially R. Chaligné. We also thank L. Lanier for helpful discussions. K. Murphy and T. Murphy provided mice critical to this study. T. Holmes and Y. Bryceson shared sequencing data from their study. We acknowledge the use of the Integrated Genomics Operation Core, funded by the National Cancer Institute Cancer Center Support Grant (P30CA008748),

Cycle for Survival and the Marie-Josée and Henry R. Kravis Center for Molecular Oncology. J.N.F. is a Cancer Research Institute Irvington Fellow supported by the Cancer Research Institute (award CRI4186). K.C.H. and J.-B.L.L were supported by funding from the National Institutes of Health (R01 AI150999, R01HL155741, U01AI069197). J.C.S. was supported by the Ludwig Center for Cancer Immunotherapy, the American Cancer Society, the Burroughs Wellcome Fund and the National Institutes of Health (AI100874, AI130043, AI155558 and P30CA008748).

Data availability

All published data generated and supporting the findings of this study have been deposited to NCBI's GEO or European Genome–Phenome Archive as described. scRNA-seq and ChIP-seq data generated in this study have been deposited at GEO under accession code GSE236556. Source data are provided with this paper.

References

1. Lau CM et al. Epigenetic control of innate and adaptive immune memory. Nat. Immunol. 19, 963–972 (2018). [PubMed: 30082830]
2. Mujal AM, Delconte RB & Sun JC Natural killer cells: from innate to adaptive features. Annu. Rev. Immunol. 39, 417–447 (2021). [PubMed: 33902312]
3. Sun JC, Beilke JN & Lanier LL Adaptive immune features of natural killer cells. Nature 457, 557–561 (2009). [PubMed: 19136945]
4. Adams EJ et al. Structural elucidation of the m157 mouse cytomegalovirus ligand for Ly49 natural killer cell receptors. Proc. Natl Acad. Sci. USA 104, 10128–10133 (2007). [PubMed: 17537914]
5. Arase H, Mocarski ES, Campbell AE, Hill AB & Lanier LL Direct recognition of cytomegalovirus by activating and inhibitory NK cell receptors. Science 296, 1323–1326 (2002). [PubMed: 11950999]
6. Nabekura T et al. Costimulatory molecule DNAM-1 is essential for optimal differentiation of memory natural killer cells during mouse cytomegalovirus infection. Immunity 40, 225–234 (2014). [PubMed: 24440149]
7. Madera S et al. Type I IFN promotes NK cell expansion during viral infection by protecting NK cells against fratricide. J. Exp. Med. 213, 225–233 (2016). [PubMed: 26755706]
8. Madera S & Sun JC Cutting edge: stage-specific requirement of IL-18 for antiviral NK cell expansion. J. Immunol. 194, 1408–1412 (2015). [PubMed: 25589075]
9. Sun JC et al. Proinflammatory cytokine signaling required for the generation of natural killer cell memory. J. Exp. Med. 209, 947–954 (2012). [PubMed: 22493516]
10. Wiedemann GM et al. Divergent role for STAT5 in the adaptive responses of natural killer cells. Cell Rep. 33, 108498 (2020). [PubMed: 33326784]
11. Wiedemann GM et al. Deconvoluting global cytokine signaling networks in natural killer cells. Nat. Immunol. 22, 627–638 (2021). [PubMed: 33859404]
12. Hammer Q, Ruckert T & Romagnani C Natural killer cell specificity for viral infections. Nat. Immunol. 19, 800–808 (2018). [PubMed: 30026479]
13. Zhao GN, Jiang DS & Li H Interferon regulatory factors: at the crossroads of immunity, metabolism, and disease. Biochim. Biophys. Acta 1852, 365–378 (2015). [PubMed: 24807060]
14. Huber M & Lohoff M IRF4 at the crossroads of effector T-cell fate decision. Eur. J. Immunol. 44, 1886–1895 (2014). [PubMed: 24782159]
15. Mittrucker HW et al. Requirement for the transcription factor LSIRF/IRF4 for mature B and T lymphocyte function. Science 275, 540–543 (1997). [PubMed: 8999800]
16. Duncan GS, Mittrucker HW, Kagi D, Matsuyama T & Mak TW The transcription factor interferon regulatory factor-1 is essential for natural killer cell function in vivo. J. Exp. Med. 184, 2043–2048 (1996). [PubMed: 8920893]
17. Lohoff M et al. Deficiency in the transcription factor interferon regulatory factor (IRF)-2 leads to severely compromised development of natural killer and T helper type 1 cells. J. Exp. Med. 192, 325–336 (2000). [PubMed: 10934221]

18. Ogasawara K et al. Requirement for IRF-1 in the microenvironment supporting development of natural killer cells. Nature 391, 700–703 (1998). [PubMed: 9490414]
19. Mace EM et al. Biallelic mutations in IRF8 impair human NK cell maturation and function. J. Clin. Invest. 127, 306–320 (2017). [PubMed: 27893462]
20. Adams NM et al. Transcription factor IRF8 orchestrates the adaptive natural killer cell response. Immunity 48, 1172–1182 (2018). [PubMed: 29858012]
21. Beaulieu AM, Zawislak CL, Nakayama T & Sun JC The transcription factor Zbtb32 controls the proliferative burst of virus-specific natural killer cells responding to infection. Nat. Immunol. 15, 546–553 (2014). [PubMed: 24747678]
22. Bravo Garcia-Morato M et al. New human combined immunodeficiency caused by interferon regulatory factor 4 (IRF4) deficiency inherited by uniparental isodisomy. J. Allergy Clin. Immunol. 141, 1924–1927 (2018). [PubMed: 29408330]
23. Man K et al. The transcription factor IRF4 is essential for TCR affinity-mediated metabolic programming and clonal expansion of T cells. Nat. Immunol. 14, 1155–1165 (2013). [PubMed: 24056747]
24. Geary CD et al. Non-redundant ISGF3 components promote NK cell survival in an auto-regulatory manner during viral infection. Cell Rep. 24, 1949–19576 (2018). [PubMed: 30134157]
25. Schlums H et al. Cytomegalovirus infection drives adaptive epigenetic diversification of NK cells with altered signaling and effector function. Immunity 42, 443–456 (2015). [PubMed: 25786176]
26. Rückert T, Lareau CA, Mashreghi MF, Ludwig LS & Romagnani C Clonal expansion and epigenetic inheritance of long-lasting NK cell memory. Nat. Immunol. 23, 1551–1563 (2022). [PubMed: 36289449]
27. Holmes TD et al. The transcription factor Bcl11b promotes both canonical and adaptive NK cell differentiation. Sci. Immunol. 6, eabc9801 (2021). [PubMed: 33712472]
28. Kallies A et al. A role for Blimp1 in the transcriptional network controlling natural killer cell maturation. Blood 117, 1869–1879 (2011). [PubMed: 21131593]
29. Yao S et al. Interferon regulatory factor 4 sustains CD8(+) T cell expansion and effector differentiation. Immunity 39, 833–845 (2013). [PubMed: 24211184]
30. Flommersfeld S et al. Fate mapping of single NK cells identifies a type 1 innate lymphoid-like lineage that bridges innate and adaptive recognition of viral infection. Immunity 54, 2288–2304 (2021). [PubMed: 34437840]
31. Finak G et al. MAST: a flexible statistical framework for assessing transcriptional changes and characterizing heterogeneity in single-cell RNA sequencing data. Genome Biol. 16, 278 (2015). [PubMed: 26653891]
32. Intlekofer AM et al. Effector and memory CD8+ T cell fate coupled by T-bet and eomesodermin. Nat. Immunol. 6, 1236–1244 (2005). [PubMed: 16273099]
33. Omilusik KD et al. Transcriptional repressor ZEB2 promotes terminal differentiation of CD8+ effector and memory T cell populations during infection. J. Exp. Med. 212, 2027–2039 (2015). [PubMed: 26503445]
34. van Helden MJ et al. Terminal NK cell maturation is controlled by concerted actions of T-bet and Zeb2 and is essential for melanoma rejection. J. Exp. Med. 212, 2015–2025 (2015). [PubMed: 26503444]
35. Zook EC et al. Transcription factor ID2 prevents E proteins from enforcing a naive T lymphocyte gene program during NK cell development. Sci. Immunol. 3, eaao2139 (2018). [PubMed: 29703840]
36. Riggan L et al. The transcription factor Fli1 restricts the formation of memory precursor NK cells during viral infection. Nat. Immunol. 23, 556–567 (2022). [PubMed: 35288713]
37. Milner JJ et al. Runx3 programs CD8(+) T cell residency in non-lymphoid tissues and tumours. Nature 552, 253–257 (2017). [PubMed: 29211713]
38. Wang D et al. The transcription factor Runx3 establishes chromatin accessibility of *cis*-regulatory landscapes that drive memory cytotoxic T lymphocyte formation. Immunity 48, 659–674 (2018). [PubMed: 29669249]
39. Delconte RB et al. The helix-loop-helix protein ID2 governs NK cell fate by tuning their sensitivity to interleukin-15. Immunity 44, 103–115 (2016). [PubMed: 26795246]

40. Loftus RM et al. Amino acid-dependent cMyc expression is essential for NK cell metabolic and functional responses in mice. Nat. Commun. 9, 2341 (2018). [PubMed: 29904050]
41. Frost JN et al. Evaluation of perturbed iron-homeostasis in a prospective cohort of patients with COVID-19. Wellcome Open Res. 7, 173 (2022). [PubMed: 35935705]
42. Frost JN et al. Plasma iron controls neutrophil production and function. Sci. Adv. 8, eabq5384 (2022). [PubMed: 36197985]
43. Bonadonna M et al. Iron regulatory protein (IRP)-mediated iron homeostasis is critical for neutrophil development and differentiation in the bone marrow. Sci. Adv. 8, eabq4469 (2022). [PubMed: 36197975]
44. Li P et al. BATF-JUN is critical for IRF4-mediated transcription in T cells. Nature 490, 543–546 (2012). [PubMed: 22992523]
45. Kaech SM & Cui W Transcriptional control of effector and memory $CD8^+$ T cell differentiation. Nat. Rev. Immunol. 12, 749–761 (2012). [PubMed: 23080391]
46. Laidlaw BJ & Cyster JG Transcriptional regulation of memory B cell differentiation. Nat. Rev. Immunol. 21, 209–220 (2021). [PubMed: 33024284]
47. Adams NM et al. Cytomegalovirus infection drives avidity selection of natural killer cells. Immunity 50, 1381–1390 (2019). [PubMed: 31103381]
48. Grassmann S et al. Distinct surface expression of activating receptor Ly49H drives differential expansion of NK cell clones upon murine cytomegalovirus infection. Immunity 50, 1391–1400 (2019). [PubMed: 31103380]
49. Gordon SM et al. The transcription factors T-bet and Eomes control key checkpoints of natural killer cell maturation. Immunity 36, 55–67 (2012). [PubMed: 22261438]
50. Yang CY et al. The transcriptional regulators Id2 and Id3 control the formation of distinct memory CD8+ T cell subsets. Nat. Immunol. 12, 1221–1229 (2011). [PubMed: 22057289]
51. Pearce EL et al. Control of effector $CD8^+$ T cell function by the transcription factor eomesodermin. Science 302, 1041–1043 (2003). [PubMed: 14605368]
52. Sheppard S et al. Lactate dehydrogenase A-dependent aerobic glycolysis promotes natural killer cell anti-viral and anti-tumor function. Cell Rep. 35, 109210 (2021). [PubMed: 34077737]
53. Mah-Som AY et al. Reliance on Cox10 and oxidative metabolism for antigen-specific NK cell expansion. Cell Rep. 35, 109209 (2021). [PubMed: 34077722]
54. Littwitz-Salomon E et al. Metabolic requirements of NK cells during the acute response against retroviral infection. Nat. Commun. 12, 5376 (2021). [PubMed: 34508086]
55. Ganz T & Nemeth E Iron homeostasis in host defence and inflammation. Nat. Rev. Immunol. 15, 500–510 (2015). [PubMed: 26160612]
56. Lane DJ et al. Cellular iron uptake, trafficking and metabolism: key molecules and mechanisms and their roles in disease. Biochim. Biophys. Acta 1853, 1130–1144 (2015). [PubMed: 25661197]
57. Tussiwand R et al. Compensatory dendritic cell development mediated by BATF–IRF interactions. Nature 490, 502–507 (2012). [PubMed: 22992524]
58. Ciofani M et al. A validated regulatory network for Th17 cell specification. Cell 151, 289–303 (2012). [PubMed: 23021777]
59. Glasmacher E et al. A genomic regulatory element that directs assembly and function of immune-specific AP-1-IRF complexes. Science 338, 975–980 (2012). [PubMed: 22983707]
60. Kim S et al. High amount of transcription factor IRF8 engages AP1-IRF composite elements in enhancers to direct type 1 conventional dendritic cell identity. Immunity 53, 759–774 (2020). [PubMed: 32795402]
61. Consortium IRFI et al. A multimorphic mutation in IRF4 causes human autosomal dominant combined immunodeficiency. Sci. Immunol. 8, eade7953 (2023). [PubMed: 36662884]
62. Thouenon R et al. A neomorphic mutation in the interferon activation domain of IRF4 causes a dominant primary immunodeficiency. J. Exp. Med. 220, e20221292 (2023). [PubMed: 36917008]
63. Guerin A et al. IRF4 haploinsufficiency in a family with Whipple's disease. eLife 7, e32340 (2018). [PubMed: 29537367]
64. Huntington ND, Cursons J & Rautela J The cancer-natural killer cell immunity cycle. Nat. Rev. Cancer 20, 437–454 (2020). [PubMed: 32581320]

65. Bald T, Krummel MF, Smyth MJ & Barry KC The NK cell-cancer cycle: advances and new challenges in NK cell-based immunotherapies. Nat. Immunol. 21, 835–847 (2020). [PubMed: 32690952]
66. Berrien-Elliott MM et al. Hematopoietic cell transplantation donor-derived memory-like NK cells functionally persist after transfer into patients with leukemia. Sci. Transl. Med. 14, eabm1375 (2022). [PubMed: 35196021]
67. Marin ND et al. Memory-like differentiation enhances NK cell responses to melanoma. Clin. Cancer Res. 27, 4859–4869 (2021). [PubMed: 34187852]
68. Gauthier L et al. Multifunctional natural killer cell engagers targeting NKp46 trigger protective tumor immunity. Cell 177, 1701–1713 (2019). [PubMed: 31155232]
69. Andre P et al. Anti-NKG2A mAb is a checkpoint inhibitor that promotes anti-tumor immunity by unleashing both T and NK cells. Cell 175, 1731–1743 (2018). [PubMed: 30503213]
70. Zhang Q et al. Blockade of the checkpoint receptor TIGIT prevents NK cell exhaustion and elicits potent anti-tumor immunity. Nat. Immunol. 19, 723–732 (2018). [PubMed: 29915296]
71. Liu E et al. Use of CAR-transduced natural killer cells in CD19-positive lymphoid tumors. N. Engl. J. Med. 382, 545–553 (2020). [PubMed: 32023374]
72. Knorr DA, Bachanova V, Verneris MR & Miller JS Clinical utility of natural killer cells in cancer therapy and transplantation. Semin. Immunol. 26, 161–172 (2014). [PubMed: 24618042]
73. Seo H et al. BATF and IRF4 cooperate to counter exhaustion in tumor-infiltrating CAR T cells. Nat. Immunol. 22, 983–995 (2021). [PubMed: 34282330]
74. Mercier FE, Sykes DB & Scadden DT Single targeted exon mutation creates a true congenic mouse for competitive hematopoietic stem cell transplantation: the C57BL/6-CD45.1(STEM) mouse. Stem Cell Rep. 6, 985–992 (2016).
75. Fodil-Cornu N et al. Ly49h-deficient C57BL/6 mice: a new mouse cytomegalovirus-susceptible model remains resistant to unrelated pathogens controlled by the NK gene complex. J. Immunol. 181, 6394–6405 (2008). [PubMed: 18941230]
76. Stoeckius M et al. Cell hashing with barcoded antibodies enables multiplexing and doublet detection for single cell genomics. Genome Biol. 19, 224 (2018). [PubMed: 30567574]
77. Azizi E et al. Single-cell map of diverse immune phenotypes in the breast tumor microenvironment. Cell 174, 1293–1308 (2018). [PubMed: 29961579]
78. Shekhar K et al. Comprehensive classification of retinal bipolar neurons by single-cell transcriptomics. Cell 166, 1308–1323 (2016). [PubMed: 27565351]
79. Wolf FA et al. PAGA: graph abstraction reconciles clustering with trajectory inference through a topology preserving map of single cells. Genome Biol. 20, 59 (2019). [PubMed: 30890159]
80. Wolf FA, Angerer P & Theis FJ SCANPY: large-scale single-cell gene expression data analysis. Genome Biol. 19, 15 (2018). [PubMed: 29409532]
81. Subramanian A et al. Gene set enrichment analysis: a knowledge-based approach for interpreting genome-wide expression profiles. Proc. Natl Acad. Sci. USA 102, 15545–15550 (2005). [PubMed: 16199517]
82. van Dijk D et al. Recovering gene interactions from single-cell data using data diffusion. Cell 174, 716–729 (2018). [PubMed: 29961576]
83. Joshi NS et al. Inflammation directs memory precursor and short-lived effector CD8(+) T cell fates via the graded expression of T-bet transcription factor. Immunity 27, 281–295 (2007). [PubMed: 17723218]
84. Heinz S et al. Simple combinations of lineage-determining transcription factors prime cis-regulatory elements required for macrophage and B cell identities. Mol. Cell 38, 576–589 (2010). [PubMed: 20513432]
85. Zhu LJ et al. ChIPpeakAnno: a Bioconductor package to annotate ChIP-seq and ChIP-chip data. BMC Bioinform. 11, 237 (2010).
86. Zhang Y et al. Model-based analysis of ChIP-seq (MACS). Genome Biol. 9, R137 (2008). [PubMed: 18798982]
87. Ramirez F et al. deepTools2: a next generation web server for deep-sequencing data analysis. Nucleic Acids Res. 44, W160–W165 (2016). [PubMed: 27079975]

88. Hammer Q et al. Peptide-specific recognition of human cytomegalovirus strains controls adaptive natural killer cells. Nat. Immunol. 19, 453–463 (2018). [PubMed: 29632329]

89. Love MI, Huber W & Anders S Moderated estimation of fold change and dispersion for RNA-seq data with DESeq2. Genome Biol. 15, 550 (2014). [PubMed: 25516281]

90. Lareau CA et al. Massively parallel single-cell mitochondrial DNA genotyping and chromatin profiling. Nat. Biotechnol. 39, 451–461 (2021). [PubMed: 32788668]

91. Stuart T, Srivastava A, Madad S, Lareau CA & Satija R Single-cell chromatin state analysis with Signac. Nat. Methods 18, 1333–1341 (2021). [PubMed: 34725479]

92. Korsunsky I et al. Fast, sensitive and accurate integration of single-cell data with Harmony. Nat. Methods 16, 1289–1296 (2019). [PubMed: 31740819]

93. Stuart T et al. Comprehensive integration of single-cell data. Cell 177, 1888–1902 (2019). [PubMed: 31178118]

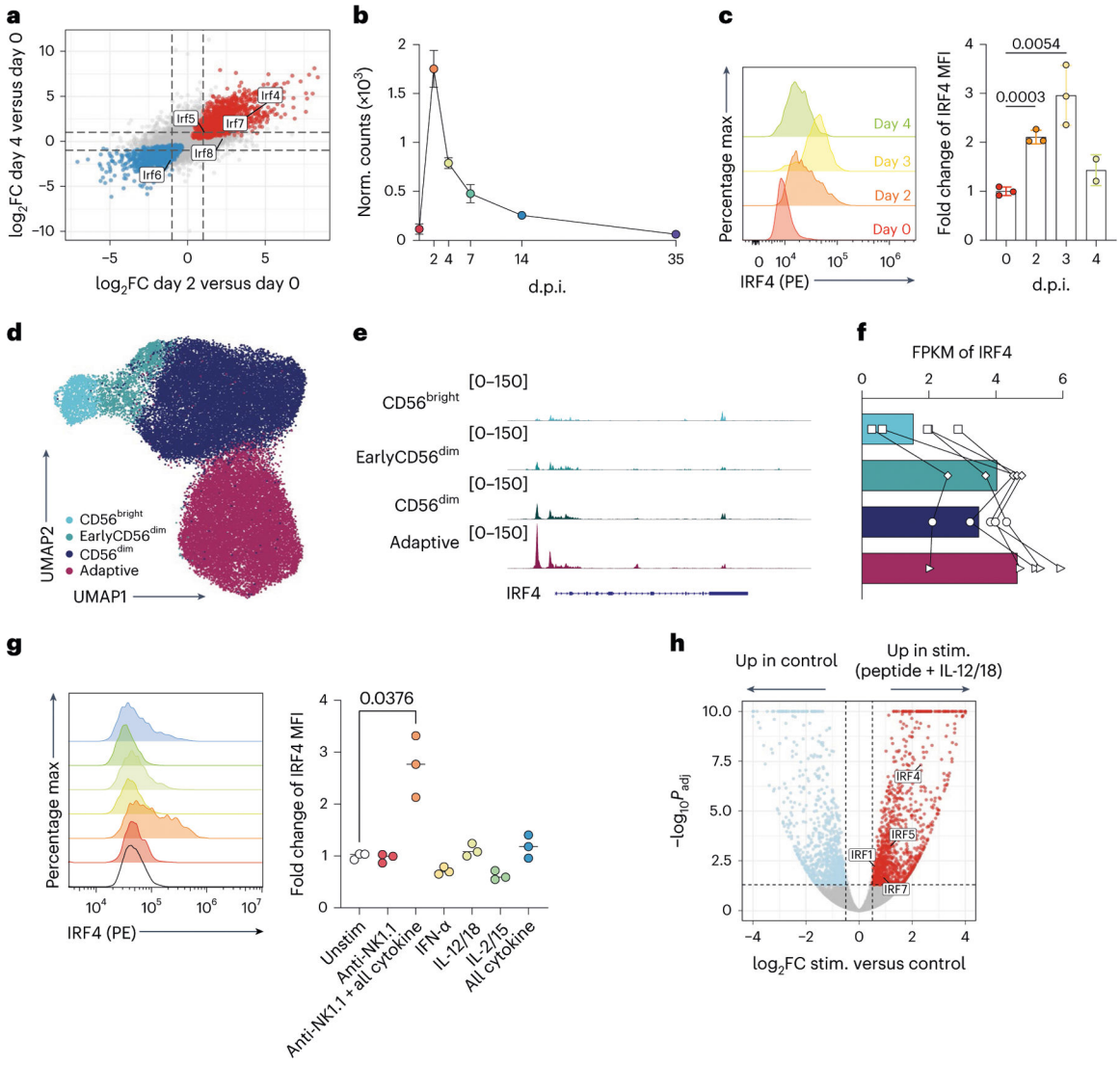

Fig. 1 |. Dynamic regulation of IRF4 in NK cells in response to viral infection.

a, Scatter-plot comparing the expression of IRF family members that are differentially expressed on days 2 and 4 PI versus day 0 in Ly49H$^+$ NK cells by RNA-seq analysis. Points highlighted in red and blue indicate genes that are upregulated and downregulated, respectively, on day 2 versus day 0 and day 4 versus day 0 ($P_{adj} < 0.05$). **b**, Kinetics of RNA-seq normalized reads for *Irf4* transcripts in Ly49H$^+$ NK cells throughout the course of MCMV infection ($n = 2$ biological replicates per time point). **c**, Representative flow cytometric histogram of IRF4 expression in splenic Ly49H$^+$ NK cells in MCMV-infected mice (left) and fold change of IRF4 mean fluorescent intensity (MFI) compared to uninfected mice (right) ($n = 3$ biological replicates for day 0, 2 and 3 and $n = 2$ biological replicates for day 4). **d**, UMAP embedding of scATAC-seq data from human NK cells of HCMV$^+$ or HCMV$^-$ healthy donors. **e**, Coverage plot of the *IRF4* locus from defined human NK cell subsets as in **d**. **f**, RNA-seq reads for *IRF4* expression from human NK cell subsets represented as fragments per kilobase of transcript per million mapped reads (FPKM) ($n = 5$). CD56^{bright} (CD56^{bright}CD16^{dim}), early CD56^{dim}

($CD56^{dim}NKG2A^{+}KIR^{-}CD57^{-}$), $CD56^{dim}$ ($CD56^{dim}NKG2A^{-}self\text{-}KIR^{+}CD57^{+}$), adaptive $NKG2C^{+}$ ($CD56^{dim}CD16^{+}NKG2C^{+}CD7^{low}NKp30^{low}CD57^{+}$). **g**, Representative histogram of IRF4 expression of sorted naive splenic NK cells after an overnight stimulation with the indicated stimuli. IRF4 induction is displayed as FC of IRF4 MFI over unstimulated condition ($n = 3$ per group). **h**, Volcano plot of RNA-seq data from human NK cells stimulated with HCMV UL-40 peptide + IL-12/18 versus control peptide. Red and blue points represent DEGs ($P_{adj} < 0.05$ and $|\log_2 FC| > 0.5$) in stimulated and control conditions, respectively. Data are represented as mean ± s.e.m. and are representative of, or pooled from, at least two independent experiments. A two-tailed unpaired *t*-test was used for **g**. Statistical analysis was not derived from groups with $n < 3$.

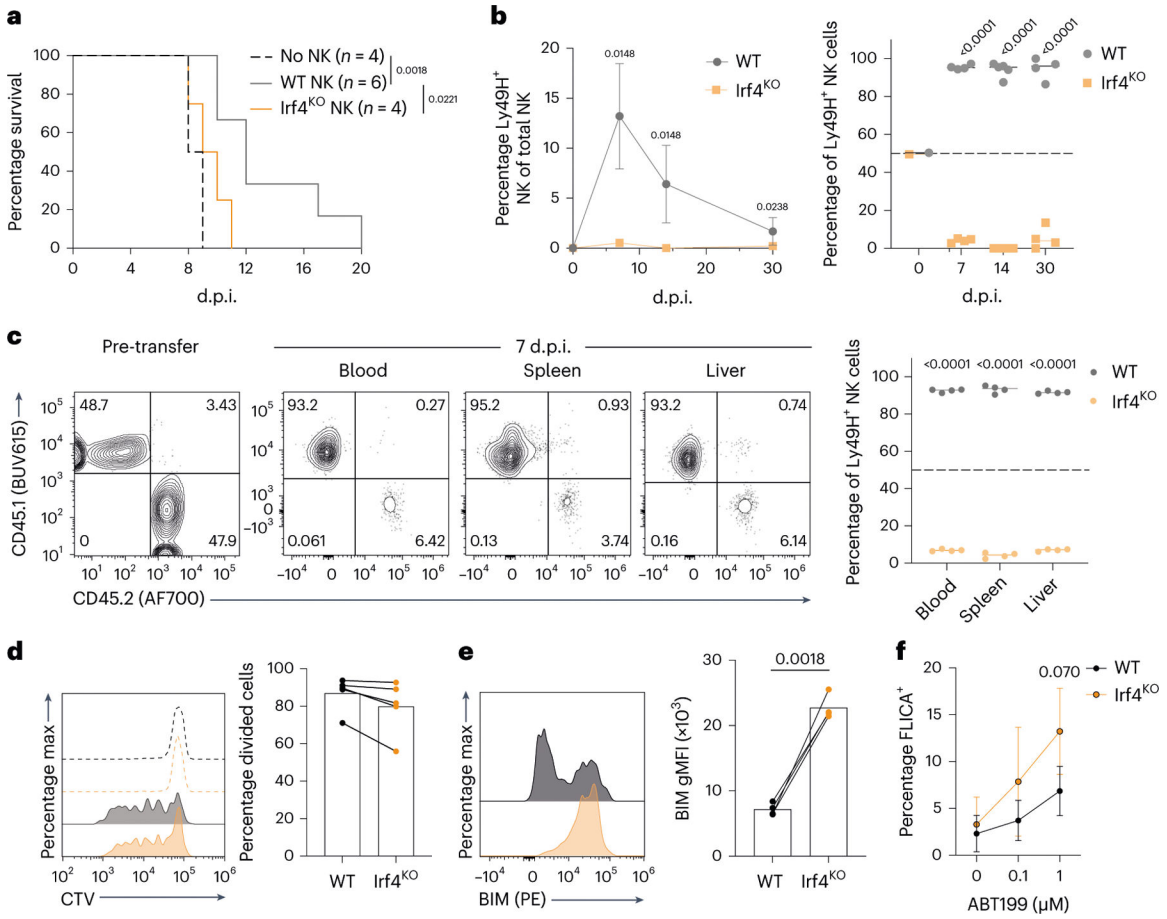

Fig. 2 |. IRF4 is required for NK cell-mediated protection against MCMV.

a, Kaplan–Meier survival curves from *Rag2*$^{-/-}$ *Il2rg*$^{-/-}$ mice transferred with WT Ly49H^{+} NK, *Irf4*$^{-/-}$Ly49H^{+} NK or no NK cells (*n* as indicated). **b**, Percentage of Ly49H^{+} NK cells from adoptive co-transfer of WT (CD45.1) and *Irf4*$^{-/-}$ (CD45.2) NK cells into Ly49H-deficient mice from the blood throughout the course of MCMV infection (left) and percent chimerism of WT versus *Irf4*$^{-/-}$ transferred Ly49H^{+} NK cells (right) (*n* = 4 biological replicates). **c**, Representative flow plots gated on transferred WT (CD45.1) and *Irf4*$^{-/-}$ (CD45.2) Ly49H^{+} NK cells on day 7 in different tissues (left) and the percent chimerism of WT and *Irf4*$^{-/-}$ NK cells within transferred Ly49H^{+} NK cells between different tissues (*n* = 4 biological replicates per group). **d**, Representative histogram of CTV dilution on day 0 and day 4 PI gated on transferred Ly49H^{+} NK cells (left). Dashed gray and orange lines represent WT and *Irf4*$^{-/-}$ NK cells on day 0, respectively; solid gray and orange lines represent WT and Irf4$^{-/-}$ NK cells on day 4 PI, respectively. Percentage of transferred NK cells that have divided at least once (*n* = 5 biological replicates per group) (right). **e**, Representative histogram of BIM expression on day 5 PI from splenic WT or *Irf4*$^{-/-}$Ly49H^{+} NK cells (left) and BIM gMFI (right) (*n* = 4 biological replicates). gMFI, geometric mean fluorescence intensity. **f**, Percentage of FLICA^{+} (marking activated caspase) WT or *Irf4*$^{-/-}$Ly49H^{+} NK cells taken from day 5 PI WT:*Irf4*$^{-/-}$ mBMC splenocytes upon ex vivo treatment with ABT199 (BCL2 inhibitor) (*n* = 3 biological replicates in each condition). Data are represented as mean ± s.e.m. and are representative of, or pooled from, at least

two independent experiments. For statistical testing, a log-rank test was used for **a** and a two-tailed paired *t*-test was used for **b**–**f** and adjusted for multiple comparisons for **b** and **c**.

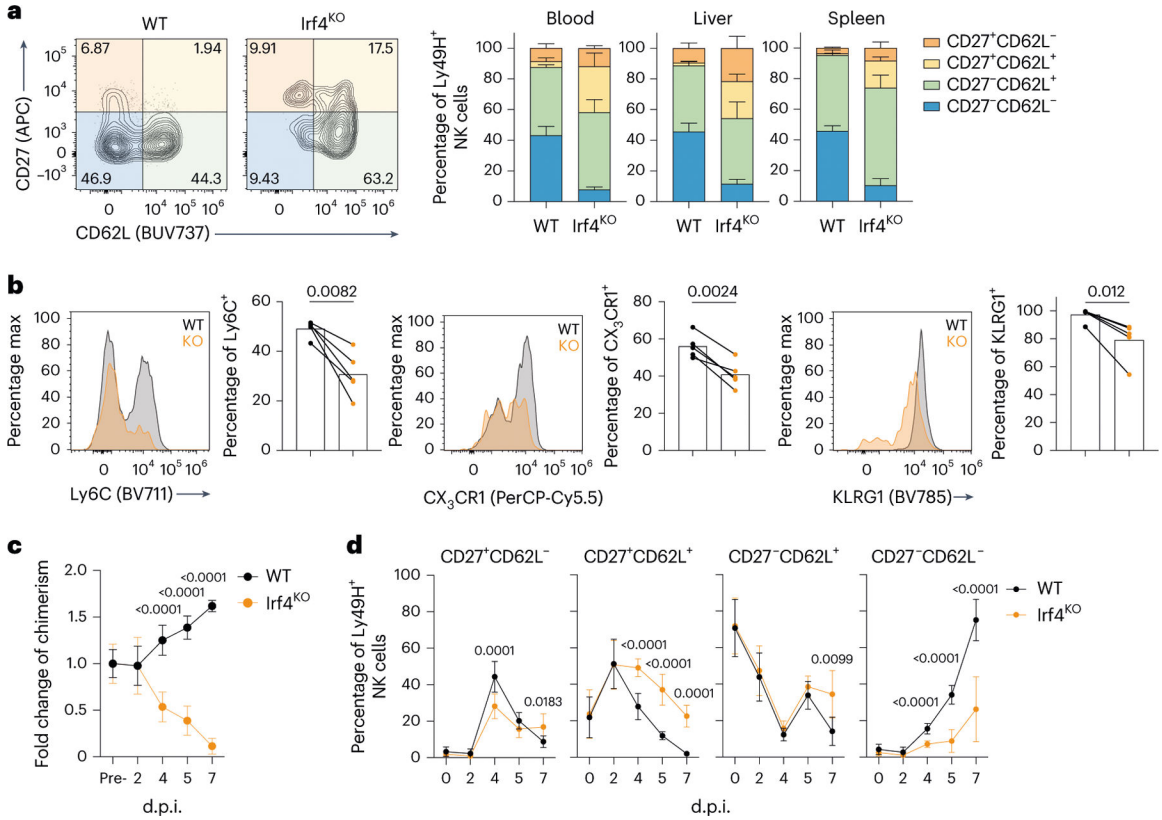

Fig. 3 |. IRF4 is required for adaptive NK cell differentiation during viral infection.

a, Representative flow plots showing CD62L and CD27 expression of transferred WT or *Irf4*$^{-/-}$Ly49H^{+} NK cells on day 7 PI (left). Percentage of NK cell subset based on CD62L and CD27 expression of transferred cells on day 7 PI in the blood, liver and spleen (right) (n = 5 biological replicates in blood and spleen and n = 4 biological replicates in liver). **b**, Representative histogram and percentages of Ly6C, CX_3CR1 and KLRG1 of transferred WT or *Irf4*$^{-/-}$ Ly49H^{+} NK cells on day 7 PI from spleens of MCMV-infected mice (n = 5 per group). **c**, Fold change of chimerism between splenic WT and *Irf4*$^{-/-}$Ly49H^{+} NK cells upon infection of WT:*Irf4*$^{-/-}$ mBMC with MCMV from day 0, 2, 4, 5 and 7 PI (n = 6 biological replicates for day 0 and 7, n = 5 biological replicates for day 2, n = 7 and 8 biological replicates for day 4 and 5, respectively). **d**, Kinetics of different subsets of splenic WT and *Irf4*$^{-/-}$Ly49H^{+} NK cells from WT:*Irf4*$^{-/-}$ mBMC during MCMV infection setting based on CD62L and CD27 expression from day 0 to 7 PI (n = 6 biological replicates for day 0 and 7, n = 7 biological replicates for day 2 and n = 8 biological replicates for day 4 and 5, respectively). Data are represented as mean ± s.e.m. and are representative of or pooled from at least two independent experiments. A two-tailed paired t-test was performed for **b**–**d** and adjusted for multiple comparisons for **c** and **d**.

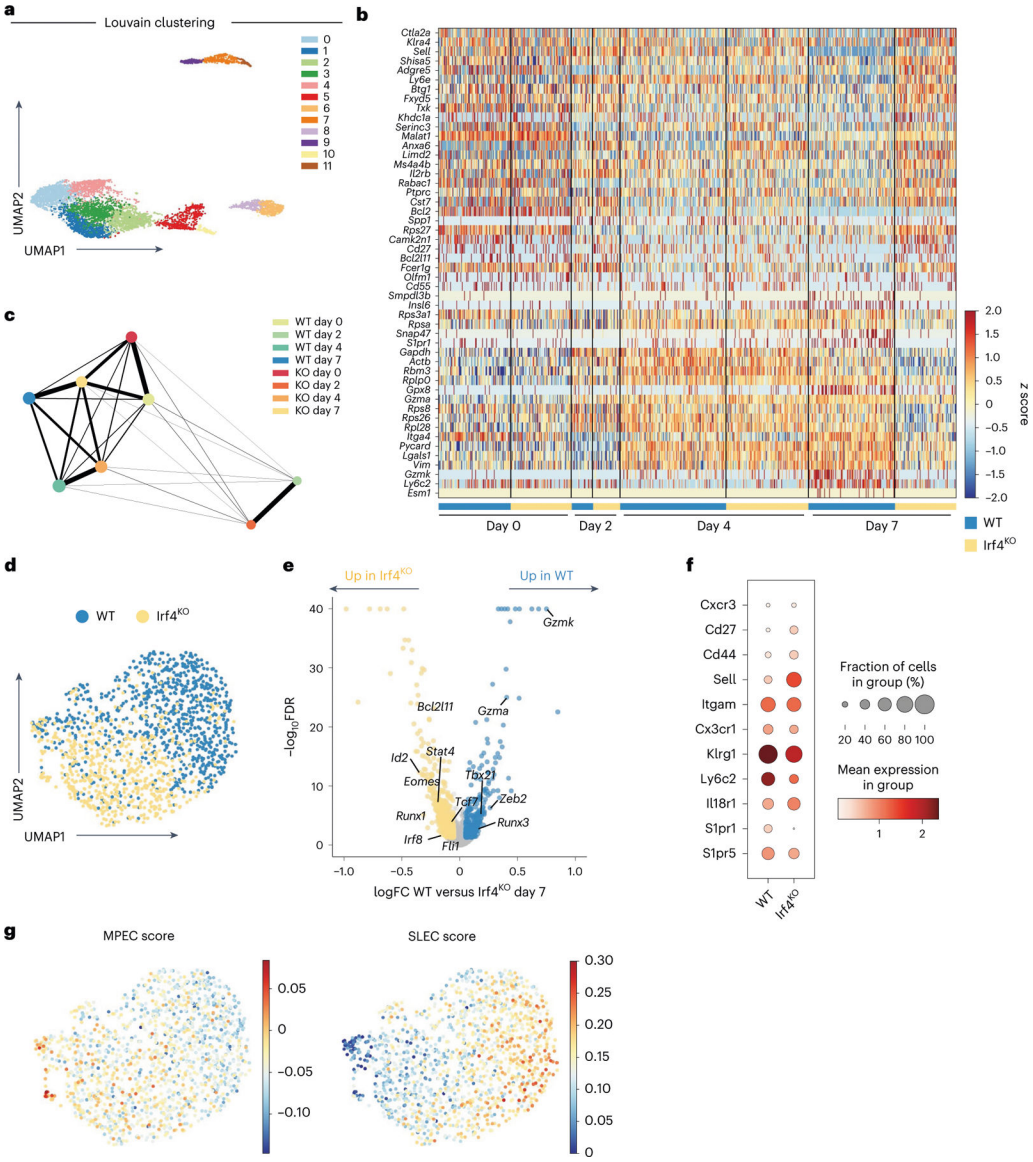

Fig. 4 |. IRF4 controls the transcriptional program of effector NK cells.

a, WT and *Irf4*$^{-/-}$ Ly49H^{+} NK cells were sorted on day 0, 2, 4 and 7 following MCMV infection and single-cell RNA-sequencing performed on multiplexed samples. UMAP embedding of scRNA-seq colored by Louvain clusters (k_n = 30). **b**, Top 50 DEGs between WT and *Irf4*$^{-/-}$Ly49H^{+} NK cells during MCMV shown as *z* score of normalized reads. **c**, PAGA network analysis based on scRNA-seq data from WT versus *Irf4*$^{-/-}$Ly49H^{+} NK cells scRNA-seq. **d**, UMAP embedding of WT and *Irf4*$^{-/-}$Ly49H^{+} NK cells on day 7 from clusters 1 and 3 in **a**. **e**, Volcano plot of scRNA-seq as determined by MAST between WT and *Irf4*$^{-/-}$Ly49H^{+} NK cells on day 7 PI. Blue and yellow points represent significant genes (FDR < 0.05) that are upregulated in WT or *Irf4*$^{-/-}$Ly49H^{+} NK cells, respectively. Highlighted genes are effector genes and/or factors known to be important for NK cell differentiation/maturation. **f**, Dot plot of scRNA-seq for maturation markers between WT and *Irf4*$^{-/-}$Ly49H^{+} NK cells on day 7 PI shown as mean normalized expression and percent

of cell fraction within the group. **g**, UMAP plot from **d** as MPEC or SLEC gene signature module scores.

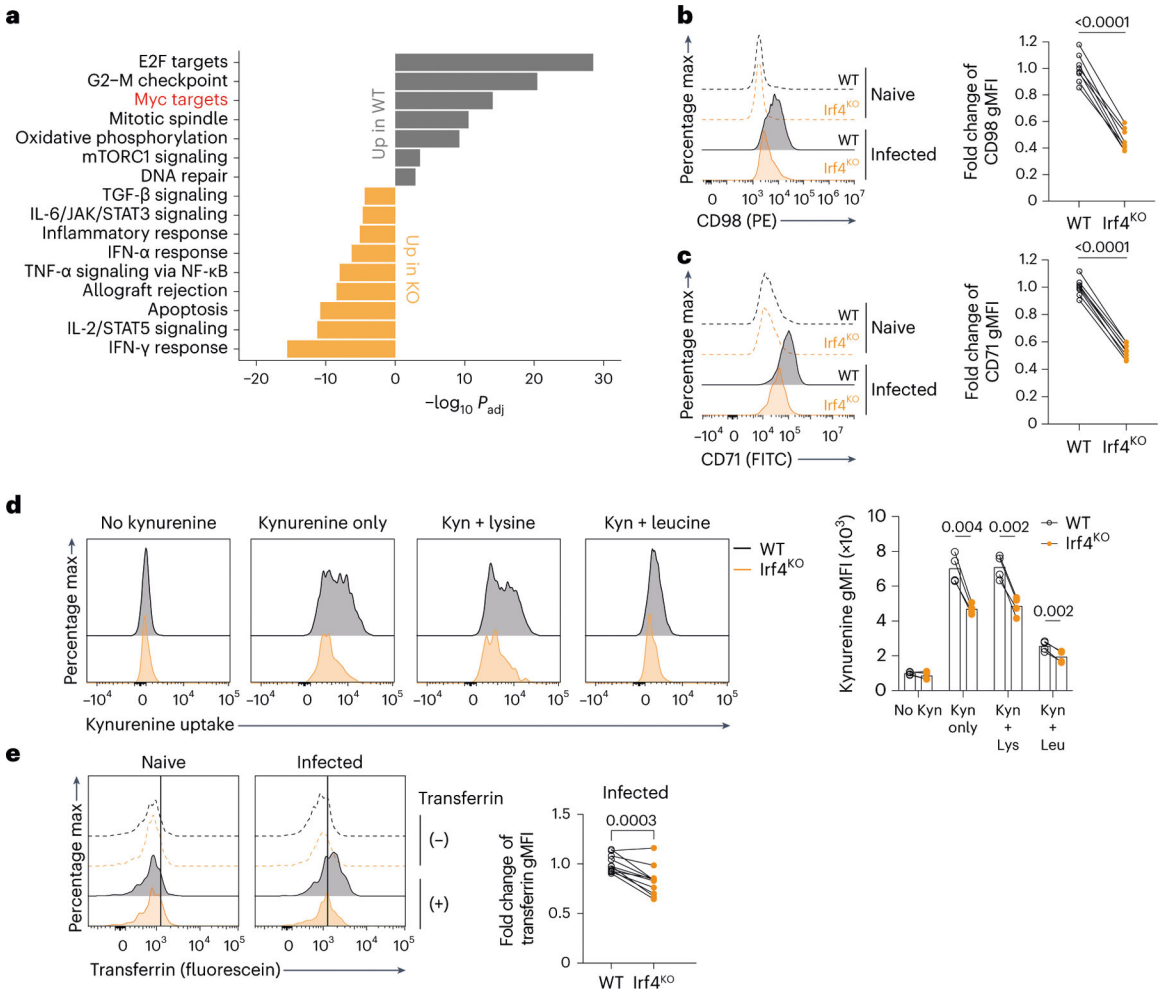

Fig. 5 |. IRF4 regulates nutrient uptake in antiviral NK cells.

a, GSEA pathway analysis of DEGs between WT and *Irf4*$^{-/-}$Ly49H^{+} cells on day 7 PI, from scRNA-seq experiment in Fig. 4. **b**, Representative histograms of CD98 expression between naive splenic WT and *Irf4*$^{-/-}$Ly49H^{+} NK cells (dashed lines) or day 5 PI (solid lines). Data are represented as FC gMFI from WT cells taken from day 5 MCMV-infected mice (n = 8 biological replicates). **c**, Representative histograms of CD71 expression between naive splenic WT and *Irf4*$^{-/-}$Ly49H^{+} NK cells (dashed lines) or day 5 PI (solid lines). Data are represented as FC gMFI from WT cells taken from day 5 MCMV-infected mice (n = 8 biological replicates). **d**, Representative histogram and gMFI of kynurenine uptake by splenic WT or *Irf4*$^{-/-}$Ly49H^{+} NK cells taken from day 5 PI. Kyn + lysine (Lys) was added as a non-competitive control and Kyn + leucine (Leu) acted as a competitive control (n = 4 biological replicates in each condition). **e**, Representative histogram and gMFI of transferrin uptake assay from naive or day 5 PI splenic WT or *Irf4*$^{-/-}$Ly49H^{+} NK cells (n = 11 biological replicates). Data are represented as mean ± s.e.m. and are representative of or pooled from at least two independent experiments. A two-tailed paired t-test was performed for **b**–**e** and adjusted for multiple comparisons for **d**.

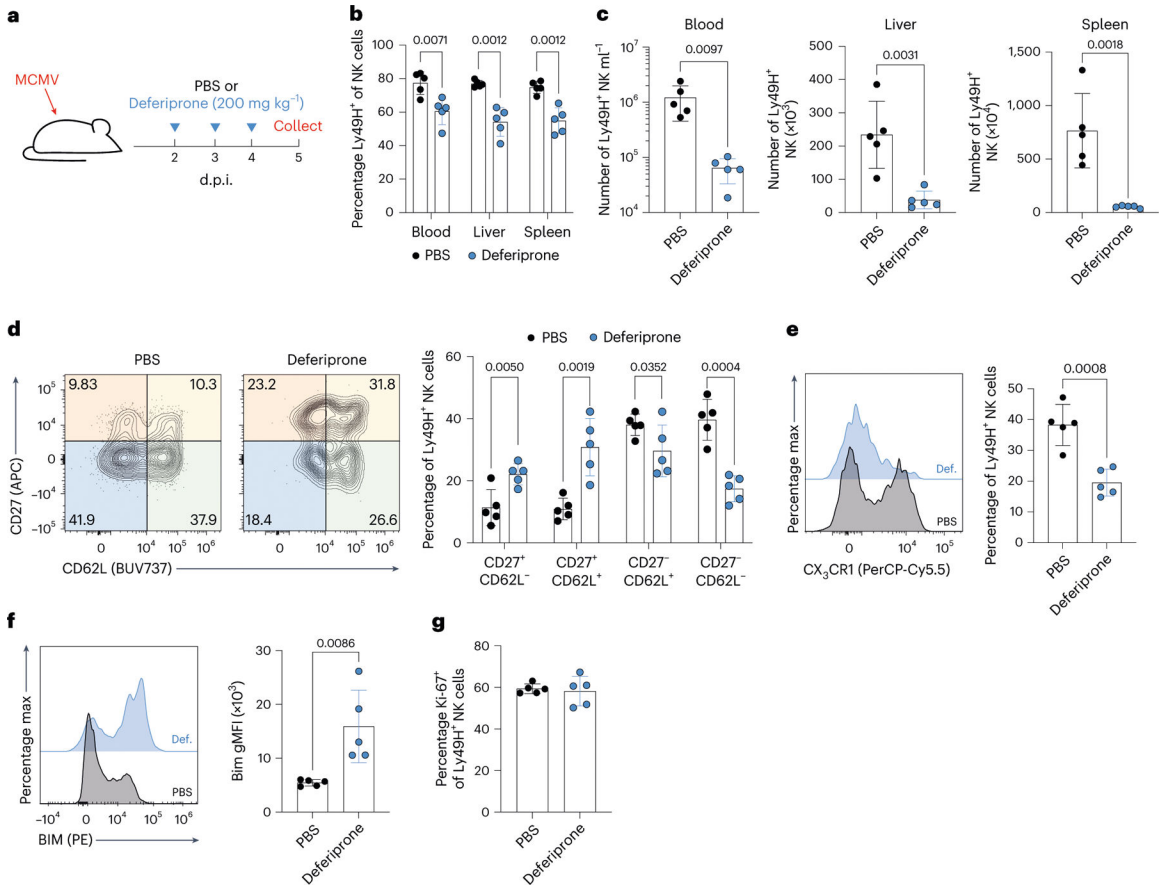

Fig. 6 |. Disruption of iron homeostasis impairs the adaptive NK cell response to viral infection.

a, Experimental schematic of PBS or deferiprone i.p. treatment during MCMV infection in WT mice. **b**, Percent expansion of blood, liver and splenic Ly49H$^+$ NK cells in PBS- or deferiprone-treated mice following MCMV infection ($n = 5$ per group). **c**. Numeric quantification of Ly49H$^+$ NK cells in the blood, liver or spleen of PBS- or deferiprone-treated mice on day 5 PI ($n = 5$ biological replicates). **d**, Representative flow plots of CD62L and CD27 expression between PBS- or deferiprone-treated on day 5 PI. Data are represented as percentage of each subset within the Ly49H$^+$ NK cell population ($n = 5$ biological replicates). **e**, Representative histogram and percentage of CX_3CR1 expression gated on Ly49H$^+$ NK cells from PBS- or deferiprone-treated mice ($n = 5$ biological replicates). **f**, Representative histogram and gMFI of BIM expression on Ly49H$^+$ NK cells between PBS- or deferiprone-treated mice ($n = 5$ biological replicates). **g**, Percentage of Ki-67$^+$ of Ly49H$^+$ NK cells from PBS- or deferiprone-treated mice ($n = 5$ biological replicates). Data are represented as mean ± s.e.m. and are representative of, or pooled from, at least two independent experiments. $n = 5$ per group. A two-tailed unpaired *t*-test adjusted for multiple comparison was performed for **b** and **d** and a two-tailed unpaired *t*-test was performed for **c** and **e**–**g**.

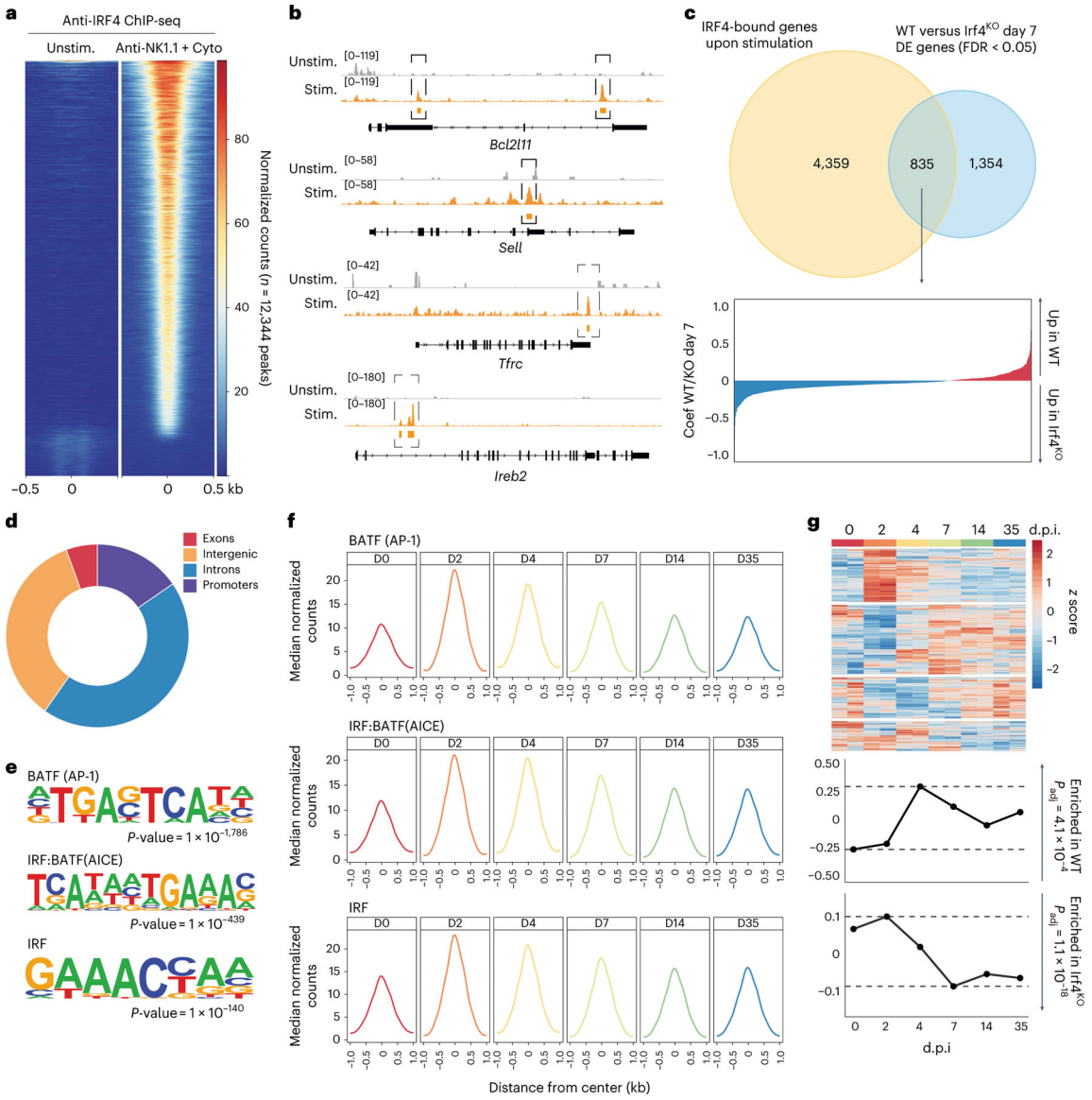

Fig. 7 |. IRF4 directly regulates adaptive features of NK cells.

a, Normalized count heat map of IRF4 binding upon anti-NK1.1 + cytokines (IFN-α + IL-12/18 + IL-2/15) stimulation or IL-15 alone at +0.5 kb from the peak summit (n = 12,344 peaks). **b**, IGV tracks showing IRF4-binding signal between unstimulated (IL-15 alone, gray) or stimulated (anti-NK1.1 + cytokines, orange) conditions in *Bcl2l11*, *Sell*, *Tfrc* and *Ireb2* loci. Regions highlighted in dashed boxes represent called IRF4 peaks by MACS2 in stimulated condition. **c**, Top: Venn diagram comparing IRF4-bound genes in stimulated condition and DEGs between WT versus *Irf4*$^{-/-}$Ly49H^{+} NK cells on day 7 PI from scRNA-seq. Bottom: distribution of IRF4-bound DEGs between WT versus *Irf4*$^{-/-}$Ly49H^{+} NK shown as fold change as analyzed by MAST. **d**, Proportion of IRF4 genome-wide occupancy within the exon, intergenic, intronic and promoter regions. **e**, Enriched de novo motifs found by HOMER on IRF4-bound regions upon stimulation. *P* values were calculated by HOMER (Methods). **f**, Metacoverage of IRF4-bound accessible regions that

contain the indicated motifs in Ly49H$^+$ NK cells upon MCMV infection as assessed by ATAC-seq. Data are shown as median of normalized counts. **g**, Top: the *z* score of DEGs that contain AICE motifs in Ly49H$^+$ NK cells during MCMV infection. Bottom: average of scaled log-normalized counts of AICE-motif-containing genes enriched in either WT or *Irf4*$^{-/-}$Ly49H$^+$ NK cells (Methods) throughout the course of MCMV. Adjusted *P* values (P_{adj}) were calculated by 'geseca' function of the fgsea package (Methods).